ATMOSPHERIC CHARACTERIZATION OF THE HOT JUPITER KEPLER-13Ab

The Astrophysical Journal, 788:92 (19pp), 2014 June 10 doi:10.1088/0004-637X/788/1/92

ATMOSPHERIC CHARACTERIZATION OF THE HOT JUPITER KEPLER-13Ab

Avi Shporer[1,2,17], Joseph G. O'Rourke[1], Heather A. Knutson[1], Gyula M. Szabó[3,4,5], Ming Zhao[6], Adam Burrows[7], Jonathan Fortney[8], Eric Agol[9], Nicolas B. Cowan[10], Jean-Michel Desert[11], Andrew W. Howard[12], Howard Isaacson[13], Nikole K. Lewis[14,15,17], Adam P. Showman[14], and Kamen O. Todorov[16]
[1] Division of Geological and Planetary Sciences, California Institute of Technology, Pasadena, CA 91125, USA
[2] Jet Propulsion Laboratory, California Institute of Technology, 4800 Oak Grove Drive, Pasadena, CA 91109, USA
[3] ELTE Gothard Astrophysical Observatory, H-9704 Szombathely, Szent Imre herceg út 112, Hungary
[4] Konkoly Observatory, Research Centre of Astronomy and Earth Sciences, Hungarian Academy of Sciences, H-1121 Budapest, Konkoly Th. M. út 15-17, Hungary
[5] Gothard-Lendület Research Team, H-9704 Szombathely, Szent Imre herceg út 112, Hungary
[6] Department of Astronomy and Astrophysics, 525 Davey Laboratory, The Pennsylvania State University, University Park, PA 16802, USA
[7] Department of Astrophysical Sciences, Princeton University, Princeton, NJ 08544, USA
[8] Department of Astronomy and Astrophysics, University of California, Santa Cruz, CA 95064, USA
[9] Department of Astronomy, University of Washington, Seattle, WA 98195, USA
[10] Center for Interdisciplinary Exploration and Research in Astrophysics and Department of Physics and Astronomy, Northwestern University, 2131 Tech Drive, Evanston, IL 60208, USA
[11] CASA, Department of Astrophysical and Planetary Sciences, University of Colorado, 389-UCB, Boulder, CO 80309, USA
[12] Institute for Astronomy, University of Hawaii, 2680 Woodlawn Drive, Honolulu, HI 96822, USA
[13] University of California, Berkeley, CA 94720, USA
[14] Department of Planetary Sciences and Lunar and Planetary Laboratory, The University of Arizona, Tucson, AZ 85721, USA
[15] Department of Earth, Atmospheric and Planetary Sciences, Massachusetts Institute of Technology, Cambridge, MA 02139, USA
[16] Institute for Astronomy, ETH Zürich, Wolfgang-Pauli-Strasse 27, 8093 Zürich, Switzerland
Received 2014 January 29; accepted 2014 April 11; published 2014 May 27

ABSTRACT

Kepler-13Ab (= KOI-13.01) is a unique transiting hot Jupiter. It is one of very few known short-period planets orbiting a hot A-type star, making it one of the hottest planets currently known. The availability of *Kepler* data allows us to measure the planet's occultation (secondary eclipse) and phase curve in the optical, which we combine with occultations observed by warm *Spitzer* at 4.5 μm and 3.6 μm and a ground-based occultation observation in the K_s band (2.1 μm). We derive a day-side hemisphere temperature of 2750 $\pm$ 160 K as the effective temperature of a black body showing the same occultation depths. Comparing the occultation depths with one-dimensional planetary atmosphere models suggests the presence of an atmospheric temperature inversion. Our analysis shows evidence for a relatively high geometric albedo, $A_g = 0.33^{+0.04}_{-0.06}$. While measured with a simplistic method, a high A_g is supported also by the fact that the one-dimensional atmosphere models underestimate the occultation depth in the optical. We use stellar spectra to determine the dilution, in the four wide bands where occultation was measured, due to the visual stellar binary companion $1\farcs15 \pm 0\farcs05$ away. The revised stellar parameters measured using these spectra are combined with other measurements, leading to revised planetary mass and radius estimates of $M_p = 4.94$–$8.09\,M_J$ and $R_p = 1.406 \pm 0.038\,R_J$. Finally, we measure a *Kepler* midoccultation time that is 34.0 $\pm$ 6.9 s earlier than expected based on the midtransit time and the delay due to light-travel time and discuss possible scenarios.

Key words: planetary systems – stars: early-type – stars: individual (Kepler-13, BD+46 2629) – techniques: photometric – techniques: spectroscopic

Online-only material: color figures, machine-readable tables

1. INTRODUCTION

The study of exoplanetary atmospheres is one of the most exciting aspects of the discovery of planets outside the solar system. When the system is in a favorable edge-on geometric configuration, the atmosphere of the unseen planet can be probed by measuring the decrease in observed flux during planetary transit (the planet moves across the disk of its host star) or planetary occultation (secondary eclipse, when the planet moves behind the star), at different wavelengths. This approach favors large, hot, gas giant planets with large atmospheric scale heights, commonly known as hot Jupiters. This class of planets earns its name by having a radius about the radius of Jupiter while orbiting at short orbital periods, close in to their host star. Tidal interaction is expected to lock (synchronize) the planet spin with the orbit, keeping the same planetary hemisphere constantly facing the star (a permanent day side) and the other hemisphere constantly facing away from the star (a permanent night side). Such planets do not exist in the solar system, so only by probing the atmospheres of these distant worlds can we learn about atmospheric processes and atmospheric chemistry in such exotic environments.

The number of hot Jupiters whose atmospheres were studied using occultations is continuously rising and currently number in the several dozens. As the field transitions from the detailed study of individual objects to the characterization of a significant sample, several correlations or patterns are emerging. Several authors (e.g., Cowan & Agol 2011; Perna et al. 2012; Perez-Becker & Showman 2013) have noticed that among the hot Jupiters, the hottest planets tend to have a low albedo and poor heat redistribution from the day-side hemisphere to the night-side hemisphere, pointing to a decreased advection efficiency. Knutson et al. (2010) noticed that planets with an inversion layer in their upper atmosphere, where temperature increases with

[17] NASA Sagan Fellow.

decreasing pressure, tend to orbit chromospherically quiet (i.e., nonactive) stars, whereas planets with no inversion layer orbit chromospherically active stars. The inversion can be attributed to an absorber in the upper atmosphere that is being destroyed by UV radiation from chromospherically active stars (Knutson et al. 2010). However, the occurrence of atmospheric inversions might also be related to atmospheric chemical composition, specifically the C-to-O elemental abundance ratio compared to the solar composition value (Madhusudhan et al. 2011; Madhusudhan 2012). Another interesting correlation involving chromospheric activity was identified by Hartman (2010), who showed that planets with increased surface gravity tend to orbit stars with increased chromospheric activity.

The patterns mentioned above are not fully explained. Gaining a better understanding of these patterns requires testing them with a larger sample and studying planets at extreme environments or with different characteristics, while observing over a wide range of wavelengths and obtaining a rough characterization of their spectrum. Kepler-13Ab is such an extremely hot Jupiter, orbiting an A-type star every 1.76 days at a distance of only 0.034 AU. The close proximity to a hot, early-type star makes this planet one of the hottest currently known. With an irradiation at the planetary surface over 15,000 times that of Jupiter in the solar system, the expected blackbody temperature of Kepler-13Ab is up to over 3000 K (for zero albedo and no heat redistribution from the day to night sides), comparable to the smallest stars, motivating the study of its atmosphere. Moreover, main-sequence A-type stars are inaccessible to spectroscopic radial velocity (RV) planet searches because their spectrum does not allow high-precision RV measurements, making this a unique opportunity to study a planet in a short-period orbit around a main-sequence A-type star. The only other currently known hot Jupiter orbiting a bright A-type star is WASP-33b (Collier Cameron et al. 2010; Kovács et al. 2013), although that system is not in the *Kepler* field, and the host star's pulsating nature hampers the measurement of occultation depths.

Here we carry out an atmospheric characterization of Kepler-13Ab by measuring its occultation in four different wavelength bands, from the infrared (IR; *Spitzer*/Infrared array camera (IRAC) 4.5 μm and 3.6 μm), through the near-IR (NIR; K_s band), to the optical (*Kepler*). We also analyze the *Kepler* phase curve and obtain Keck/high-resolution echelle spectrometer (HIRES) spectra that result in revised parameters for the objects in the system. We describe the analysis of our various data sets in Section 2. In Section 3, we study the planet's atmosphere, and in Section 4, we discuss our results.

1.1. The Kepler-13 System

The Kepler-13 system is a four-body system, as far as we currently know. A high angular resolution image is shown in Figure 1, taken from the publicly accessible *Kepler* Community Follow-up Observing Program (CFOP) website.[18] The image was obtained in the K_s (K short) band with the Palomar high angular resolution observer (PHARO) camera (Hayward et al. 2001) and the adaptive optics system mounted on the Palomar 200 inch (5 m) Hale telescope (P200). The two bright components seen in Figure 1 are two A-type stars, where the brighter one, the primary (Kepler-13A), hosts a transiting planet (Kepler-13Ab[19]), while the fainter one, the secondary (Kepler-13B), is orbited by a third star (Kepler-13BB) of

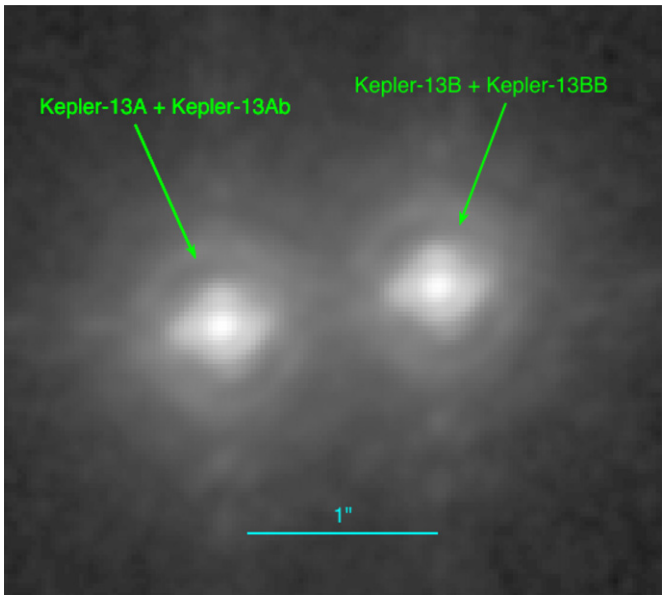

Figure 1. High angular resolution adaptive optics imaging of the Kepler-13 system, obtained with P200/PHARO in the K_s band. North is up and east is to the left. The system is a visual binary, composed of two A-type stars at a sky-projected separation of $1''.15 \pm 0''.05$. The brighter one, the primary, Kepler-13A, is to the east (left) and is the planet host. The fainter component, the secondary, Kepler-13B, is to the west (right) and is itself a stellar binary system, where the A-type star hosts a late-type star (Santerne et al. 2012).

(A color version of this figure is available in the online journal.)

spectral type G or later (Santerne et al. 2012). The observed angular separation between the two A-type stars was measured to be $1''.12 \pm 0''.08$ by (Adams et al. 2012; E. Adams private communication, 2014) and $1''.16 \pm 0''.06$ by Law et al. (2013), resulting in a weighted mean of $1''.15 \pm 0''.05$. The distance to the system is 530 pc (Pickles & Depagne 2010) with an uncertainty of 20% (A. Pickles, private communication, 2014), giving a sky-projected separation of 610 ± 120 AU.

The availability of *Kepler* data for a short-period planet transiting an A-type star in a bright ($V = 9.95$ mag) hierarchical system makes it an interesting astrophysical laboratory. It is the first planet whose mass was estimated using photometric light curves (Shporer et al. 2011; Mazeh et al. 2012; Mislis & Hodgkin 2012; Esteves et al. 2013; Placek et al. 2013), and the first star–planet system where the star's obliquity was measured by modeling the asymmetric transit light curve due to stellar gravity darkening (Szabó et al. 2011; Barnes et al. 2011). In addition, orbital precession was also identified (Szabó et al. 2012, 2014).

2. OBSERVATIONS AND DATA ANALYSIS

All data used in this work are publicly available, either through dedicated archives of the relevant observatory or by request from the authors.

In all of our photometric light curve analyses, from the IR (*Spitzer*/IRAC) through the NIR (P200/wide-field infrared camera/K_s) to the optical (*Kepler*), we assume that the measured flux is the combined flux from the two stars in the visual binary system (see Figure 1), i.e., the two stars are fully blended together. We first analyze the data as is, without correcting for the dilution, and derive the measured occultation depth. Only then do we correct the measured depth, by estimating the amount of dilution, and derive the undiluted or corrected occultation depth. As shown in Section 2.6, we estimate the dilution at

[18] https://cfop.ipac.caltech.edu/

[19] In the literature it is occasionally referred to as simply Kepler-13b.

each observed wavelength band by using Keck/HIRES resolved spectra of the two stars along with spectral models.

Before moving to the description of the analysis of individual data sets we note that throughout this paper we have estimated the scatter in a given sample using the median absolute deviation from the median, also called median absolute deviation (MAD), defined as

$$\mathrm{MAD} = \mathrm{median}_j \left| X_j - \mathrm{median}_i(X_i) \right|. \quad (1)$$

This statistic is more robust than the root mean square because it is less sensitive to outliers and hence provides a more reliable estimate of the standard deviation (StD) of the underlying distribution (e.g., Hoaglin et al. 1983). The StD, or 1σ, is calculated as

$$\sigma = 1.4826 \cdot \mathrm{MAD}. \quad (2)$$

In addition, we note that when estimating the scatter in a given sample or when performing model fitting, we removed outliers iteratively while recalculating the scatter in each iteration until no outliers are left. The threshold, n, in units of σ, which is the distance from the mean beyond which outliers were removed, was chosen to give an expectation value of less than 0.5 for the total number of outlier data points that exist in the sample, assuming a Gaussian distribution. This way, the threshold depends on the sample size because as a sample grows larger so does the probability of data points having values further away from the median. This criteria can be written as the following inequality, which n must satisfy given a sample of size N with mean μ and standard deviation σ:

$$1 - \frac{1}{2N} < \frac{1}{\sigma\sqrt{2\pi}} \int_{\mu-n\sigma}^{\mu+n\sigma} e^{-\frac{(x-\mu)^2}{2\sigma^2}} dx. \quad (3)$$

For the sample sizes in this paper, ranging from about 1000 up to about 50,000, the minimal value for n ranges from 3.5 to 4.5. Removing data points in this way ensures a negligible decrease in the measured scatter due to outlier removal, following a possible removal of data points belonging to the same Gaussian distribution but located at the distribution tails. We have also performed a visual inspection to verify that points identified as outliers do not appear to belong to the same Gaussian distribution.

2.1. Spitzer 4.5 μm Data

Our analysis was done on *Spitzer* Basic Calibrated Data produced by IRAC pipeline version S18.18.0 and obtained as part of Program ID 80219 (PI: H. Knutson). Our *Spitzer*/IRAC photometric and model fitting pipeline was implemented in Matlab, and we make our code publicly available.[20]

We obtained a total of 3,973 full-frame exposures, with an effective integration time of 4.4 s and a median cycle time of 7.2 s. The entire data set spans 7.83 hr.

Before analyzing the data we visually examined the $5\farcm2 \times 5\farcm2$ IRAC full-frame images to verify that there are no bright stars other than the target within the intended photometric aperture or sky annulus. We also verified that the visual binary nature of the target does not affect its point-spread function (PSF) shape and that its width is comparable to that of other stars in the frame's field of view. The latter is expected because the IRAC pixel scale of $1\farcs2$ per pixel is comparable to the angular distance between the visual binary components, so the two stars are fully blended on *Spitzer*/IRAC pixels.

[20] http://gps.caltech.edu/~shporer/spitzerphot/

2.1.1. Preprocessing

First, we extracted the midexposure Barycentric Julian Date (BJD) of all images using the information in the image keyword headers. We used the BMJD_OBS keyword timestamps, which is in UTC time, and added the leap seconds given by the difference between the ET_OBS and UTCS_OBS keyword timestamps. Next we added half the cycle time, given by the FRAMTIME header keyword, to get the midexposure BJD:

$$\mathrm{BJD} = \mathrm{BMJD\_OBS} + (\mathrm{ET\_OBS} - \mathrm{UTCS\_OBS}) + \mathrm{FRAMTIME}/2 + 2{,}400{,}000.5, \quad (4)$$

where ET_OBS, UTCS_OBS, and FRAMTIME were converted to units of days. Equation (4) gives an approximate BJD_TDB to better than one second (Eastman et al. 2010), which is sufficient for our needs.

Using the target's median pixel position across all images, we extracted the 80×80 pixel region centered on the target from all 3,973 exposures. Those subframes were uploaded into a three-dimensional (3D) matrix, whose dimensions are X pixel coordinate, Y pixel coordinate, and image number.

Next, we removed the first 197 (= 5.0%) images in the so-called *Spitzer* "ramp," which is a fast asymptotically shaped instrumental increase in observed flux at the beginning of the observation. The cause for this fast initial ramp is not completely clear, but it may be due to telescope pointing settling or charge trapping. It has become common practice to trim out the initial part of the data, ranging from a few tens of minutes up to an hour or more, in order to minimize the scatter in the residuals from the best-fit model (e.g., Knutson et al. 2012; Todorov et al. 2012; Lewis et al. 2013). The data removed here includes the first 23 minutes (= 0.39 hr) of the observation.

We have examined each pixel time series separately, along the image number dimension of the 3D matrix, and marked as bad pixels those deviating by more than 5σ from the series moving median. Such pixels were marked only in the specific frames where they showed a large deviation. No alignment between subframes was done prior to this step because for this purpose the small pixel shifts between exposures, at the level of a few 0.01 pixel (see below), are negligible.

A final preprocessing step included conversion of pixel values from MJy sr^{-1} to electrons. This was done using the information in the flexible image transport system (FITS) image header keywords, as described in the IRAC Instrument Handbook, Section 6.2.[21]

2.1.2. Aperture Photometry

In each exposure, the target's central pixel position was estimated by fitting a two-dimensional Gaussian. We have also experimented with determining the central pixel position using the two-dimensional center of mass (X and Y first moments), but we achieved better results using a Gaussian fit, with a decreased scatter in the residuals from the best-fit model. The resulting scatter in central-position X and Y coordinates is ≈0.01–0.02 pixels. Figure 2 shows the X and Y pixel-position time series, where the familiar sawtooth behavior with a timescale of approximately 40 minutes is evident. This central position variation is attributed to an oscillation in *Spitzer* pointing, which when combined with the nonuniform sensitivity across IRAC pixels results in similar oscillations in the measured flux.

[21] http://irsa.ipac.caltech.edu/data/SPITZER/docs/irac/iracinstrumenthandbook/54/#_Toc296497452

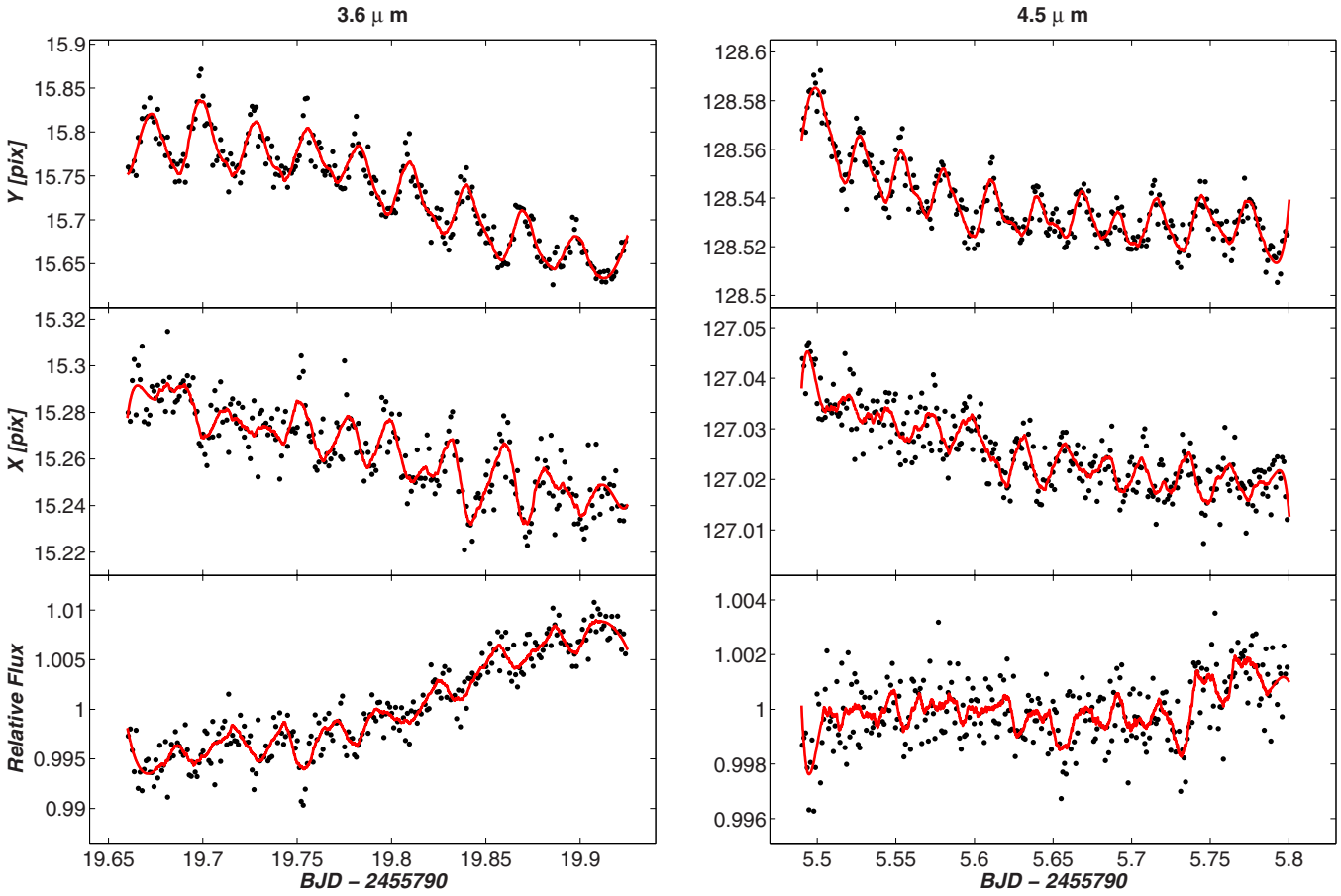

Figure 2. *Spitzer* pixel position and raw photometry binned time series, in 3.6 μm (left) and 4.5 μm (right). Top panels show the Y pixel position, middle panels the X pixel position, and bottom panels the raw photometry. The overplotted solid red line is a Savitzky–Golay smoothing, showing the familiar sawtooth pattern, with a timescale of 40 minutes.

(A color version of this figure is available in the online journal.)

We next calculated the target's flux in each image using aperture photometry with a circular aperture centered on the target and summing over the sky-subtracted pixel values of pixels within the aperture. We used a time-varying aperture calculated using the "noise pixel" parameter (Mighell 2005; Knutson et al. 2012; Lewis et al. 2013, see also IRAC Instrument Handbook Section 2.2.2[22]). In this method, we first calculate

$$\tilde{\beta} = \frac{(\Sigma_i I_i)^2}{\Sigma_i I_i^2}, \quad (5)$$

where I_i is the measured intensity in pixel i. This parameter gives the equivalent number of pixels that contribute to the point spread function, so it is an approximation for the aperture radius squared. Hence, we take the aperture radius to be

$$r_j = c_0 + c_1\sqrt{\tilde{\beta}_j}, \quad (6)$$

where r_j is the photometric aperture radius in image j, where the noise pixel parameter is $\tilde{\beta}_j$, and c_0 and c_1 are additive and multiplicative coefficients, respectively, that we optimize. Our best results were obtained for $c_1 = 1.1$ and $c_0 = 0$, meaning no additive factor. This approach resulted in a decreased scatter of the residuals from the best-fit model compared to using the same aperture for all frames.

[22] http://irsa.ipac.caltech.edu/data/SPITZER/docs/irac/iracinstrumenthandbook/5/

The sky value was estimated as the median value of pixels within an annulus centered on the target, while iteratively removing 5σ outliers. The inner and outer annulus radii for which we obtained the best results were 10 and 30 pixels, respectively, although varying these values by a few pixels did not change the results significantly. Typically no more than five sky pixels were identified as outliers in each image.

Images where a bad pixel (see Section 2.1.1) was identified within the photometric aperture were ignored. This removed an additional 76 exposures from further analysis, which are 1.9% of all exposures that together with the removal of the initial ramp amounts to 273 removed exposures, or 6.9%, leaving 3,700 exposures. When estimating the median sky level, bad pixels within the sky annulus were ignored. We also checked for exposures where the target's position was beyond 4σ away from the median position and did not find any.

Finally, we have median normalized the light curve measured in electrons, converting it into a relative flux light curve. We refer to this light curve as the raw photometry light curve, presented in Figure 2 bottom panel.

2.1.3. Postprocessing and Model Fitting

To model the raw photometry light curve we assumed that the relative flux is a function of pixel position and time, $F(x, y, t)$, and that light curve variability is a consequence of three processes. The first is the planetary occultation, $O(t)$, the second is the nonuniform intrapixel sensitivity, $M(x, y)$, and the

third is a long-term time-dependent process, $T(t)$.[23] Therefore our model is

$$F(x, y, t) = O(t) \times M(x, y) \times T(t). \quad (7)$$

For the occultation model, $O(t)$, we used a model based on the Mandel & Agol (2002) transit model, with the occultation depth as an additional parameter to account for the planet's luminosity. Also, the stellar limb darkening is irrelevant here, and we assume uniform surface brightness across the planet's disk. Our model assumes a circular orbit, following the expectation of complete circularization of such close-in planetary orbits (e.g., Mazeh 2008). Only the occultation depth was allowed to vary freely. The ephemeris was fixed to the one derived here (see Section 2.4), while the rest of the light curve parameters were fixed to the known values (Barnes et al. 2011) because there is not enough signal-to-noise in the *Spitzer* data to efficiently constrain them. For the CCD position-dependent and time-dependent components, we used polynomials:

$$M(x, y) = M_0 + M_{1,x}x + M_{2,x}x^2 + M_{1,y}y + M_{2,y}y^2, \quad (8)$$

$$T(t) = 1 + T_1 t, \quad (9)$$

where adding higher order or mixed terms (in Equation (8)) did not decrease the uncertainty on the fitted occultation depth or improve the scatter of the residuals from the best-fit model.

The above model includes seven free parameters: the occultation depth and six polynomial coefficients, which we fitted using the Monte Carlo Markov Chain (MCMC) algorithm as described in Shporer et al. (2009). We ran a total of five chains, consisting of 10^6 steps each, resulting in Gaussian distributions for the fitted parameters, after ignoring the initial 20% of each chain. We took the distribution median to be the best-fit value and the values at 84.13 and 15.87 percentiles to be the $+1\sigma$ and -1σ confidence limits, respectively. We compared the errors from the MCMC approach with errors estimated using the "residual permutation" method, referred to also as the "prayer bead" method (e.g., Gillon et al. 2007; Carter & Winn 2009), and adopted the larger of the two errors for each fit parameter. In the prayer bead method, we cyclicly shifted the residuals with respect to time and refitted. This way each fit is affected by the same correlated noise that may exist in the original data. This approach results in a distribution for each fitted parameter where we take the values at 84.13 and 15.87 percentiles to be the $+1\sigma$ and -1σ confidence limits. We verified that the distributions' medians were indistinguishable from the initial fitted values.

The resulting occultation depth is listed in Table 9 along with the scatter of the residuals, which is 2.1% larger than the expected Poisson noise. Table 9 also lists the scatter while using one-minute bins, also referred to as the photometric noise rate (PNR; e.g., Shporer et al. 2009; Fulton et al. 2011). The latter allows an easy comparison between light curves obtained with different instruments, with different exposure times and cycle times.

We have experimented with other models and fitting methods to confirm our results. First, we replaced the Mandel & Agol (2002) model with a trapezoid model because they differ only during the occultation ingress and egress phase, and the difference is up to only a few 10^{-5} in relative flux. The results we got using this model are the same as when using the original one. Another approach we tried, motivated by the sinusoidal shape of the position-dependent flux modulations (see Figure 2), was adding sinusoidal harmonics to the long-term time-dependent process ($T(t)$) while removing the $M(x, y)$ component from the model (see Equation (7)). Combined with the trapezoid model, this allows a linear least squares fitting of the entire light curve model using a single matrix inversion operation, making it efficient in computing time. However, this approach gave poorer results than the original one (larger residuals scatter with clear systematic features). A possible reason for this is that the position-dependent flux modulations are not well approximated by sinusoids.

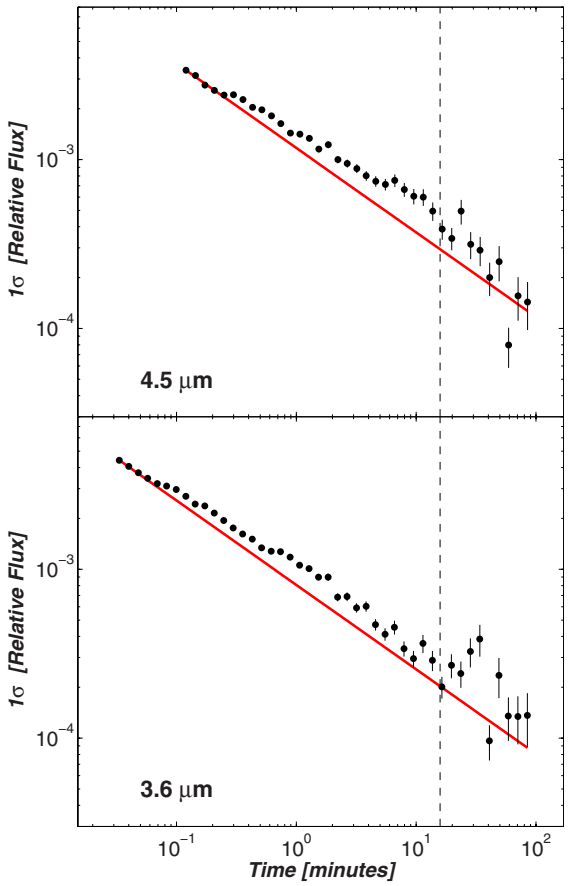

Figure 3. Light curve residuals scatter vs. bin width (black filled circles with error bars), in log-log scale, for the *Spitzer* 3.6 μm light curve (bottom) and the 4.5 μm light curve (top). The solid red line shows the expected decrease in scatter according to Poisson statistics, and the vertical dashed line marks ingress/egress duration.

(A color version of this figure is available in the online journal.)

The 4.5 μm occultation light curve is listed in Table 1 and shown in Figure 4 after removing the positional ($M(x, y)$) and long-term temporal ($T(t)$) components. In Figure 3, we plot the scatter of the residuals for a range of bin sizes. Although the scatter decreases with the inverse square root of the bin width as expected for Poisson noise, there does seem to be a correlated noise component at 1–10 minutes whose source is unknown.

2.2. *Spitzer* 3.6 μm Data

Our approach in analyzing these data was largely similar to that of the 4.5 μm analysis. Basic calibrated data files were produced by IRAC pipeline version S19.1.0, and data were

[23] This slowly varying temporal component is sometimes also referred to as a ramp in the literature, not to be confused with the fast initial ramp that is trimmed out (see Section 2.1.1).

Table 1
Spitzer 4.5 μm Light Curve

Time (BJD)	X (pixel)	Y (pixel)	Raw Rel. Flux[a]	Rel. Flux Error	Detrended Rel. Flux[b]
2455795.4900269	127.04045	128.57439	1.002220	0.003385	1.003386
2455795.4901103	127.03541	128.56319	1.002003	0.003384	1.002439
2455795.4901936	127.03748	128.56890	1.000259	0.003381	1.001002
2455795.4902723	127.03763	128.56315	0.999927	0.003381	1.000507
2455795.4903556	127.04253	128.56182	0.999790	0.003381	1.000691
2455795.4904389	127.03489	128.55481	0.997916	0.003378	0.998151
2455795.4905177	127.04364	128.55421	0.993622	0.003370	0.994462
2455795.4906010	127.04522	128.56129	0.999825	0.003381	1.000926
2455795.4906844	127.04823	128.56173	0.999433	0.003380	1.000797
2455795.4907676	127.05526	128.58094	0.997450	0.003377	1.000194

Notes. Columns include, from left to right: midexposure BJD, X coordinate, Y coordinate, raw relative flux, relative flux error, and detrended light curve after removing all variabilities except the occultation.
[a] Raw relative flux, without correcting for the intrapixel sensitivity variations.
[b] Detrended relative flux, after removing the intrapixel sensitivity variations.

(This table is available in its entirety in a machine-readable form in the online journal. A portion is shown here for guidance regarding its form and content.)

obtained as part of Program ID 80219 (PI: H. Knutson). We obtained 14,144 individual exposures spanning 7.94 hr, with an exposure time of 1.92 s and a median cycle time of 2.00 s.

We ignored the first 95 minutes (1.58 hr) of data due to the fast initial ramp, corresponding to 2,809 exposures or 19.9% of all exposures. This ramp is longer than the one we removed in the 4.5 μm data, consistent with other studies that found a longer initial ramp in this band than in 4.5 μm (e.g., Knutson et al. 2012; Lewis et al. 2013). We then rejected an additional 251 exposures, or 1.8%, with a bad pixel identified within the photometric aperture. Therefore, the number of exposures used in the analysis is 11,084, spanning 6.36 hr.

We used a two-dimensional Gaussian fit to determine the central pixel position, with a resulting scatter of 0.03 pixel and 0.07 pixel in the X and Y coordinates, respectively. The sawtooth pattern is seen in both coordinates time series, shown in Figure 2.

We determined the aperture used in each frame based on the noise pixel parameter, $\tilde{\beta}$ (see Equation (5)), where the aperture radius was taken to be $1.0 \times \sqrt{\tilde{\beta}}$, meaning $c_1 = 1.0$ and $c_0 = 0$ (see Equation (6)). The sky value was taken to be the median of pixels within an annulus between radii of 10 and 20 pixels while ignoring bad pixels.

Here our fitted model did not include a time component, meaning $T(t)$ was taken to be unity in Equation (7) because when including a linear component as a function of time (T_1 in Equation (9)) the fitted coefficient was consistent with zero, and removing it did not affect any of the results, including the residual's scatter and occultation depth. Therefore, the total number of fitted parameters was six: the occultation depth and five polynomial coefficients.

The resulting occultation depth is listed in Table 9, along with the residuals scatter and PNR. The scatter is 18.7% larger than the expected Poisson noise. Although this is more than for the 4.5 μm data, it is comparable to the excess noise level above the Poisson noise level found in other studies (e.g., Knutson et al. 2012; O'Rourke et al. 2014). The fitted occultation light curve is listed in Table 2 and plotted in Figure 4, and the residuals scatter vs. bin size is plotted in Figure 3.

2.3. Palomar 200 inch WIRC K_s Data

We observed an occultation of Kepler-13Ab in the K_s band on UT 2012 August 28 with the wide field infrared camera (WIRC; Wilson et al. 2003), mounted on the P200. The WIRC instrument has a 2,048 × 2,048 pixel detector, a pixel scale of 0.″2,487 per pixel, and a field of view of 8.′7 × 8.′7. Observation of the target field began at 03:38:04.8 UTC and ended 6.57 hr later

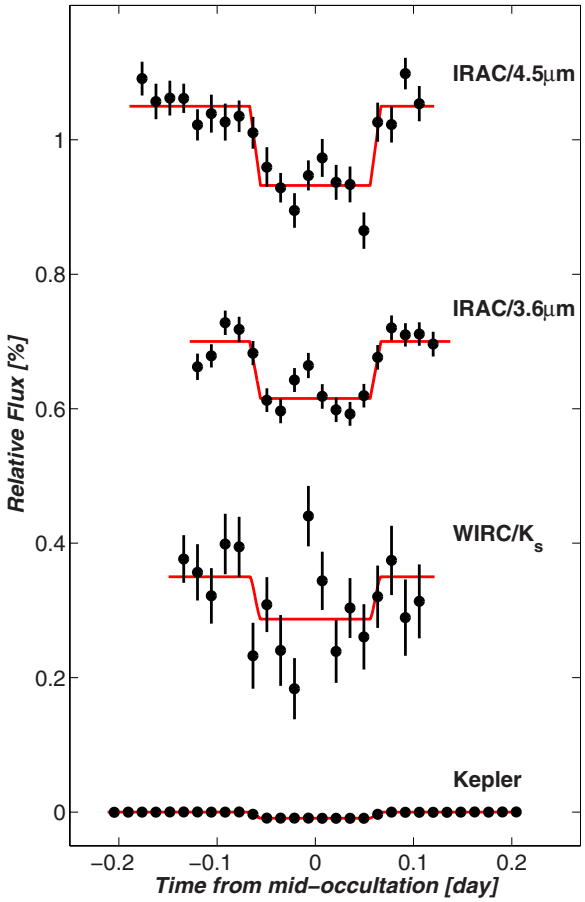

Figure 4. Binned occultation light curves in (from top to bottom) 4.5 μm and 3.6 μm (*Spitzer*), K_s band (WIRC), and optical (*Kepler*). The solid red line is the occultation model. Light curves are plotted in relative flux vs. time from midoccultation and are shifted vertically for visibility purposes. The *Kepler* occultation depth is too shallow to be seen on this scale, and the light curve is presented here just for reference, whereas it is shown in detail in Figure 5.
(A color version of this figure is available in the online journal.)

Table 2
Spitzer 3.6 μm Light Curve

Time (BJD)	X (pixel)	Y (pixel)	Raw Rel. Flux[a]	Rel. Flux Error	Detrended Rel. Flux[b]
2455809.6600049	15.28237	15.81692	0.986185	0.004432	0.991893
2455809.6600281	15.26722	15.79148	0.994718	0.004451	0.997973
2455809.6600512	15.27482	15.78554	0.995372	0.004453	0.999090
2455809.6600744	15.28386	15.78273	0.996489	0.004455	1.000945
2455809.6600975	15.28723	15.78937	1.000421	0.004464	1.005526
2455809.6601207	15.27445	15.77484	0.993759	0.004449	0.996927
2455809.6601438	15.27659	15.76911	0.998592	0.004460	1.001693
2455809.6602072	15.26584	15.74978	0.992963	0.004447	0.993996
2455809.6602304	15.25616	15.76161	0.998753	0.004460	0.999500
2455809.6602535	15.26450	15.76773	0.993252	0.004448	0.995111

Notes. Columns include, from left to right: midexposure BJD, X coordinate, Y coordinate, raw relative flux, relative flux error, and detrended light curve after removing all variabilities except the occultation.
[a] Raw relative flux, without correcting for the intrapixel sensitivity variations.
[b] Detrended relative flux, after removing the intrapixel sensitivity variations.

(This table is available in its entirety in a machine-readable form in the online journal. A portion is shown here for guidance regarding its form and content.)

while obtaining a total of 1,123 images. The first image was rejected because the telescope guiding had not yet stabilized, and so were the last three images due to increased background level as the night ended. The air mass ranged from 1.03 to 2.15 during the observation. The seeing varied throughout the night but remained $\lesssim 1''$. We began with an exposure time of 9 s but decreased the exposure time incrementally to 8 s, 7 s, and finally 6 s throughout the night to keep pixel counts in the detector's linear regime, well below saturation. We also defocused the telescope to a PSF FWHM of $\sim 2''.5$–$3''.0$ to avoid saturation and systematic errors resulting from variations in intrapixel sensitivity. As a result, Kepler-13A and Kepler-13B were completely blended in all images, and we treated the target as a single source in our photometric analysis. To minimize systematics related to imperfect flat-fielding and interpixel variations in the detector, we did not dither the telescope.

Data reduction and analysis was done using a pipeline developed specifically for WIRC data, described in more detail in O'Rourke et al. (2014), and we give only a short description here. Images were dark-subtracted and flat-fielded using the median of 18 normalized twilight flats as a single master flat field. We selected nine reference stars with median fluxes ranging from $\sim$0.09 to 1.80 times that of Kepler-13. Two bright stars in the field were ignored because their fluxes consistently saturated the detector or exceeded the linearity regime. We performed aperture photometry on each star using circular apertures with fixed radii and determined the sky background level using an annulus centered on the star's position. Aperture radius and sky annulus inner and outer radii were optimized to minimize the scatter in our final light curve model fit, yielding an aperture of 20.0 pixels and sky annulus inner and outer radii of 25.0 and 55.0 pixels, respectively. At this point we excluded another 16 images from the analysis because either pixel counts in the photometric apertures exceeded the detector's linearity regime or the total flux of the target or one of the reference stars varied by more than 3σ from the median value in the adjacent 20 frames in the time series.

For each measurement we calculated the mean of the nine reference stars and derived a single reference light curve (using the median or flux-weighted mean produced inferior results in the eventual fit). We divided the light curve for Kepler-13 by the reference light curve. Then, we fitted this normalized light curve

Table 3
WIRC K_s Light Curve

Time (BJD)	Rel. Flux	Rel. Flux Error	Detrended Rel. Flux
2456167.646833	1.00189	0.00389	0.99970
2456167.647051	1.00075	0.00389	0.99856
2456167.647264	1.00443	0.00389	1.00224
2456167.647480	1.00513	0.00389	1.00294
2456167.647907	0.99883	0.00389	0.99667
2456167.648214	1.00299	0.00389	1.00083
2456167.648473	1.00050	0.00389	0.99835
2456167.648735	0.99815	0.00389	0.99601
2456167.648994	0.99983	0.00389	0.99770
2456167.649254	1.00573	0.00389	1.00359

Notes. Columns include, from left to right: midexposure BJD, relative flux (without correcting for the long-term trend), relative flux error, and detrended light curve after removing the long-term temporal trend.

(This table is available in its entirety in a machine-readable form in the online journal. A portion is shown here for guidance regarding its form and content.)

simultaneously with a linear trend with time and a model for the occultation. As done for the *Spitzer* data, we used an occultation model based on Mandel & Agol (2002) while allowing only the occultation depth to vary freely and keeping all other occultation light curve parameters fixed. We used the ephemeris derived here (see Section 2.4) and adopt the rest of the model parameter values from the literature (Barnes et al. 2011). We fitted the light curve model using the MCMC algorithm and also used the prayer bead method where the estimated uncertainties were found to be in good agreement.

We derived an occultation depth of $0.063 \pm 0.026\%$. The residuals scatter for the best-fit solution is 0.389%, a factor of 3.56 larger than the Poisson noise limit of 0.109%. Such noise levels are similar to those obtained for other WIRC data sets (Zhao et al. 2012a, 2012b; O'Rourke et al. 2014). The WIRC/K_s occultation light curve is shown in Figure 4 and listed in Table 3.

2.4. Kepler Occultation Data

Kepler data allow a high-precision measurement of Kepler-13Ab occultation in the optical. This is thanks to the high-precision photometry, the many occultation events observed,

Table 4
Occultation Fit Parameters

Parameter	Value
Constrained parameters:	
R_p/R_s	0.0845 ± 0.0012
a/R_s	4.44 ± 0.16
b	0.317 ± 0.033
Fitted parameters:	
D_{Kepler}, ppm	90.81 ± 0.27
P, day	$1.76358799 \pm 0.00000037$
$T_{\rm occ}$, BJD	$2{,}455{,}603.448101 \pm 0.000079$

and the availability of a large amount of short-cadence data, which we used for ten quarters: Q2–Q3 and Q7–Q14.

We processed the *Kepler* short-cadence occultation data by first going through each occultation event and normalizing it using a second-degree polynomial fitted to the out-of-occultation data. Using a third-degree polynomial did not change the results. For this normalization, we used data segments centered on the occultation and spanning a total of three times the occultation itself, including out-of-occultation data before ingress and after egress spanning the same duration as the occultation. We considered only full events, meaning where the entire occultation event was observed including both pre-ingress and post-egress data. Polynomial fitting was done by iteratively removing 4σ outliers until none were identified (there were approximately 600 data points in each individual occultation light curve segment). We also removed occultation events occurring at times where the data showed strong trends, for example, near spacecraft safe modes.[24] We were left with 453 viable occultation events out of the 522 events that occurred during the above 10 quarters, which are 87% of the events. For the majority of the other 13% events, no data were obtained at all because they happened during breaks in data collection due to data downloads, quarterly spacecraft rotations, and safe modes.

Next, we fitted the data using an occultation light curve model based on the Mandel & Agol (2002) transit model as done for the *Spitzer* and WIRC data. Despite the high quality of the *Kepler* short-cadence occultation data, it cannot resolve the degeneracy between some of the model parameters, specifically the planet-to-star radii ratio, R_p/R_s, the orbital semimajor axis normalized by the stellar radius, a/R_s, the occultation impact parameter, b, and the occultation depth, D_{Kepler}. Therefore, we used Gaussian priors on three of the parameters: R_p/R_s, a/R_s, and b, and fitted as free parameters the other three model parameters, including the orbital period, P, a specific midoccultation time, $T_{\rm occ}$, and the occultation depth. Gaussian priors were taken from Barnes et al. (2011), where fitting the transit light curve resolved the three parameters R_p/R_s, a/R_s, and b.

After obtaining a preliminary fitted model in the manner described below, we repeated the fit while iteratively removing outliers beyond 5.5σ, rejecting 0.27% of the 278,901 data points. Visual inspection showed that increasing the outlier threshold did not remove some clear outliers, while decreasing it removed data points that did not seem to be outliers.

We carried out model fitting using the MCMC algorithm. We ran a total of five chains, consisting of 10^6 steps each, resulting in Gaussian distributions for the fitted parameters, after ignoring the initial 20% of each chain. We took the distributions median to be the best-fit value and the values at 84.13 and 15.87 percentiles to be the $+1\sigma$ and -1σ confidence limits, respectively. The assumed priors and fitted parameters are listed in Table 4. We also applied a prayer bead analysis to the *Kepler* occultation data that resulted in the same fitted parameter uncertainties as the MCMC approach.

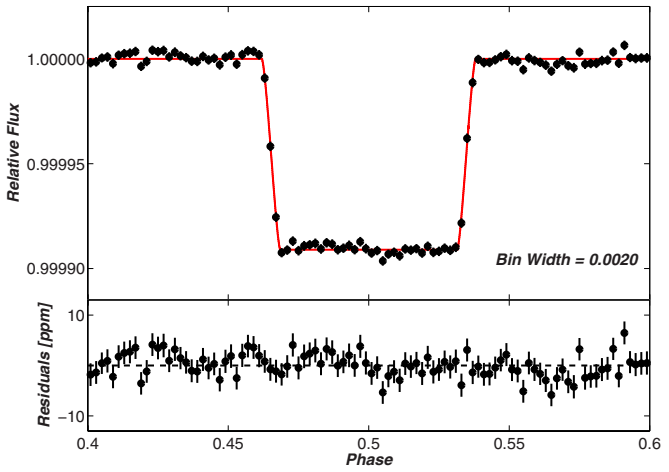

Figure 5. *Kepler* occultation light curve. Top: binned short-cadence data (black filled circles with error bars) and best-fit model (red solid line). Bottom: binned residuals (black circles) with error bars. A dashed black line is plotted at zero residuals for reference.

(A color version of this figure is available in the online journal.)

The *Kepler* phase-folded and binned light curve is presented in Figure 5 along with the fitted model and residuals. The residuals scatter is 109 ppm, and because the data is 1 minute cadence, this scatter is also the PNR of the unfolded and unbinned data (see Table 9). The PNR of the phase-folded and binned data, equivalent to the scatter of a binned light curve using 1 minute wide bins, is 5.0 ppm. We used the orbital ephemeris (P and $T_{\rm occ}$) obtained here in modeling all other data sets analyzed in this work because it is of superior precision to any ephemeris currently available in the literature.

2.4.1. Comparing Occultation to Transit Times

Model fitting the transit light curve is beyond the scope of this work because it requires carefully accounting for the gravity darkening that dominates the star's surface brightness. This results from the star's rapid rotation, which is typical of main-sequence stars of this spectral type. The rapid rotation leads to increased gravity near the stellar poles compared to the stellar equator, which results in increased surface temperature and hence increased brightness (Monnier et al. 2007). This makes the light curve deviate from the Mandel & Agol (2002) model that includes only limb darkening, as studied in detail by Barnes (2009) and identified for Kepler-13Ab by Szabó et al. (2011). In addition, due to the host star's rapid rotation, the transit light curve is expected to be distorted also by the photometric Rossiter–McLaughlin (RM) effect (Shporer et al. 2012; Groot 2012). Fortunately, a detailed model fitting of Kepler-13Ab transit was already done by Barnes et al. (2011).

Comparing the midoccultation time derived here to the midtransit time of Barnes et al. (2011) shows that the difference is consistent with half an orbital period:

$$\Delta t = T_{\rm occ} - T_{\rm tr} - P/2 = -2.6 \pm 7.5 \text{ s}, \quad (10)$$

where $T_{\rm tr}$ is the midtransit time from Barnes et al. (2011) corrected for the *Kepler* timing error.[25] We have subtracted from

[24] http://archive.stsci.edu/kepler/manuals/Data_Characteristics.pdf

[25] http://archive.stsci.edu/kepler/timing_error.html

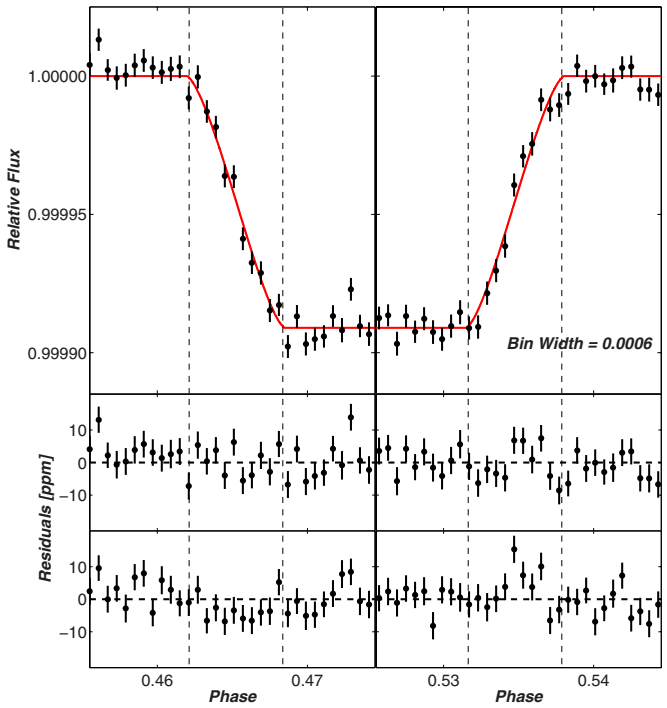

Figure 6. Top: zoomed-in view of *Kepler* phase-folded and binned light curve, as relative flux vs. phase, around ingress (left) and egress (right). Red solid line marks the fitted model. Middle: residuals, data subtracted by fitted model, of the light curves shown at the top panels. Horizontal dashed black line marks the zero residuals level, for reference. Bottom: residuals from a model shifted to the expected midoccultation time assuming a circular orbit (see Section 2.4.1). In all panels, vertical dashed black lines mark the start and end of ingress and egress (four points of contact).

(A color version of this figure is available in the online journal.)

the above result an integer number of orbital periods. Using $T_{\rm tr}$ from Batalha et al. (2013) gives only a slightly different value, of $\Delta t = +3.0 \pm 6.9$ s, within 1σ from the above, although the latter value is affected by fitting a symmetric transit light curve model to an asymmetric one, so it does not account for the effects mentioned above, which could bias the midtransit time measurement. We verified that the period derived here is consistent with the period reported in the literature based on analysis of the transit light curve (Borucki et al. 2011; Barnes et al. 2011; Batalha et al. 2013), although the period reported here is more precise.

The result presented in Equation (10) is surprising because we would expect a time difference of $+34.0 \pm 0.7$ s due to a light-travel time delay (e.g., Loeb 2005; Kaplan 2010). This expectation is based on the system parameters measured here. The difference between the expected and measured Δt equals $(+2.4 \pm 0.5) \times 10^{-4}$ of the orbital phase, close to a 5σ significance.

To investigate this further, Figure 6 shows a zoom-in view of the *Kepler* occultation light curve ingress and egress (top panels). Compared to other phases, the light curve does not show an increased scatter or correlated noise features during ingress or egress (middle panels). We also plot, in Figure 6 bottom panels, the residuals from a model with $T_{\rm occ}$ shifted to the expected time and assuming a circular orbit. Those residuals do show slightly increased correlated noise features during ingress and egress, although their significance is low. This shows visually how the midoccultation time fitted here better describes the data than the predicted midoccultation time based on the midtransit time of Barnes et al. (2011) and the light-travel time delay.

One possible explanation for the measured time shift is that the light curve ingress and egress are distorted in a way that given the quality of our data is consistent with our light curve model with a shifted midoccultation time. Such a distortion can be induced by an asymmetric planetary optical surface brightness, where the brightest region is shifted away from the substellar point. In such cases, the largest slope during ingress and egress will occur slightly earlier or later compared to cases where the planetary surface brightness is symmetric. This in turn will cause a shift in the measured midoccultation time when using a model that assumes symmetric surface brightness. Williams et al. (2006; see also de Wit et al. 2012) discuss the impact of a nonuniform surface brightness on the shape of the ingress and egress and the measured midoccultation time when fitted with a model assuming a uniform distribution. A time shift induced by a so-called hot spot or by an offset of the hottest region on the planetary surface from the substellar point was measured by Agol et al. (2010) at 8 μm for HD 189733b. In that case, the hot spot is attributed to superrotating winds near the planetary equator that shift the hot spot eastward of the substellar point (e.g., Showman & Guillot 2002; Knutson et al. 2007; Showman et al. 2009). This causes a delay in the measured $T_{\rm occ}$ whereas we find that Kepler-13Ab's occultation occurs early. The latter would be consistent with a bright region located westward of the substellar point. Demory et al. (2013) identified a nonuniform reflectivity in the optical for Kepler-7b, where the planet's most reflective region is located westward of the substellar point. This should cause the measured occultation time for that planet to occur early, although this effect is not currently detectable in the Kepler-7 system.

A different possible explanation for the time shift is a small orbital eccentricity, e. A small eccentricity adds approximately $2Pe\cos\omega/\pi$ to the time between occultation and transit (Winn 2011, Equation 33), where ω is the argument of periastron. Therefore a small eccentricity of about only 5×10^{-4} is enough to shift Δt by about half a minute while inducing a very small difference between the transit and occultation duration (Winn 2011, Equation 34) of less than 10 s. The impact of such a small eccentricity on the phased light curve shape (Section 2.5) is undetectable with our current data, so we cannot reject this possibility out of hand.

Yet another process that may affect the measured $T_{\rm occ}$ is the propagation-delay effect described by Loeb (2005), in which the planet is moving away from the observer during occultation ingress and toward the observer during egress, causing the latter to appear slightly shorter than the former. However, that effect is below the sensitivity of our data.

2.5. Kepler Phase Curve Data

Kepler's high-quality data allow us to study optical photometric modulations induced by orbital motion in star–planet systems (Loeb & Gaudi 2003; Zucker et al. 2007). For the Kepler-13A system, that was already done by several authors (Shporer et al. 2011; Mazeh et al. 2012; Mislis & Hodgkin 2012; Esteves et al. 2013; Placek et al. 2013). We carry out here an analysis of the optical phase curve using 13 quarters of long-cadence data, Q2 through Q14, comprising over four times the *Kepler* data used in previous studies. We do not use *Kepler* short-cadence data here because the higher time resolution has no additional value for the study of the sinusoidal variability along the orbital motion; using it will make the analysis unnecessarily more CPU-intensebecause of the increased amount of data points, and short-cadence data is available only for 10 quarters leading to Q14.

Table 5
Fitted Amplitudes

Component	Measured Amplitude (ppm)	Corrected Amplitude (ppm)
Two-harmonics model:		
a_{1c} – Reflection	40.00 ± 0.37	76.52 ± 1.04
a_{1s} – Beaming	4.97 ± 0.30	9.51 ± 0.58
a_{2c} – Ellipsoidal	31.40 ± 0.48	60.07 ± 1.10
a_{2s}	0.34 ± 0.36	0.65 ± 0.69
Three-harmonics model:		
a_{1c} – Reflection	40.87 ± 0.36	78.18 ± 1.04
a_{1s} – Beaming	4.94 ± 0.25	9.45 ± 0.49
a_{2c} – Ellipsoidal	31.41 ± 0.44	60.09 ± 1.03
a_{2s}	0.42 ± 0.32	0.80 ± 0.61
a_{3c}	1.66 ± 0.29	3.18 ± 0.56
a_{3s}	4.12 ± 0.20	7.88 ± 0.39

We first remove instrumental signals or trends by fitting the first four cotrending basis vectors to the data of each quarter using the Pyke Python package (Still & Barclay 2012). We then continue in a similar way to Shporer et al. (2011), where each continuous segment of data was detrended by fitting a fifth-degree polynomial while ignoring in-eclipse (in-transit and in-occultation) data and then divided by that polynomial. This did not affect the sinusoidal modulations along the orbit because the duration of each continuous segment is at least an order of magnitude longer than the orbital period. Fitting was done while iteratively rejecting 5σ outliers until none are identified. Using polynomial degrees of four and six did not change the results. We used the ephemeris obtained in the *Kepler* occultation light curve fit (see Section 2.4 and Table 4) and an eclipse duration an hour longer than the known 3.2 hr duration, to remove any long-cadence measurements partially in eclipse.

Next we analyze the variability in the phase-folded light curve. There are three well-known mechanisms through which the orbital motion of the star–planet system induces photometric modulations (e.g., Loeb & Gaudi 2003; Zucker et al. 2007; Faigler & Mazeh 2011). Those include (1) the reflection effect, due to both planetary thermal emission and reflected stellar light from the planetary surface. (2) the beaming effect, due to the varying RV of the stellar host; and (3) the ellipsoidal effect, due to tidal forces induced by the planet on the host.

We modeled the photometric modulations along the orbit using a simple model consisting of a sinusoidal component at the orbital period and two additional sinusoidal components at the first and second harmonics:

$$f(t) = a_0 + a_{1c}\cos\left(\frac{2\pi}{P}t\right) + a_{1s}\sin\left(\frac{2\pi}{P}t\right) + a_{2c}\cos\left(\frac{2\pi}{P/2}t\right) + a_{2s}\sin\left(\frac{2\pi}{P/2}t\right) + a_{3c}\cos\left(\frac{2\pi}{P/3}t\right) + a_{3s}\sin\left(\frac{2\pi}{P/3}t\right), \quad (11)$$

where f is relative flux, P the orbital period, and t is time subtracted by midtransit time, so the transit is taken to be at orbital phase zero. This model is similar to the beaming, ellipsoidal, and reflection (BEER) model (Faigler & Mazeh 2011) that we used in Shporer et al. (2011), only with an additional component at the second harmonic. In this formalism, the reflection, beaming, and ellipsoidal effects have amplitudes a_{1c}, a_{1s}, and a_{2c}, respectively. The coefficient of the sine component of the first harmonic, a_{2s}, and the coefficients of the second harmonic, a_{3c} and a_{3s}, are not associated with any of the well-known physical effects and therefore are expected to be small if not negligible, and they are included in the model for completeness. We refer to this model as the three-harmonics model. We also carried out a separate analysis without the second harmonic, meaning where a_{3c} and a_{3s} are fixed to zero, and refer to that model as the two-harmonics model.

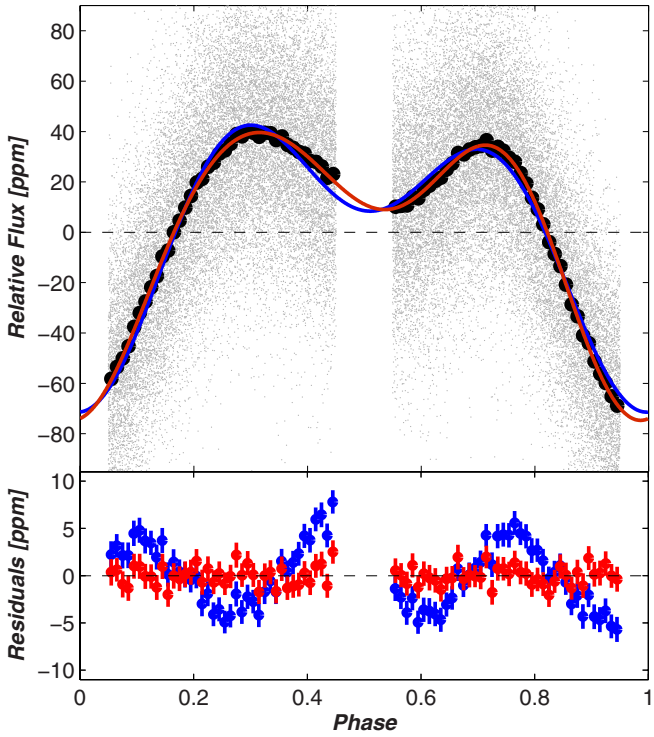

Figure 7. Top: phase-folded long-cadence *Kepler* light curve. Long cadence is marked by gray dots in the background; the binned light curve is in black filled circles (error bars comparable to marker size). The blue and red solid lines are the two-harmonics and three-harmonics model fits, respectively. Bottom: residuals (data subtracted by the model) from the two-harmonics model in blue and the three-harmonics model in red. The two-harmonics model residuals show strong correlated noise features that are not seen in the three-harmonics model residuals, indicating the latter is a better description of the data.

(A color version of this figure is available in the online journal.)

We phase folded the data using the occultation ephemeris derived here and iteratively fitted the model above while rejecting outliers until no 4.5σ outliers were left. The outlier threshold was chosen by visually examining the phased data, consisting of approximately 44,000 individual long-cadence data points, to verify that all rejected points are clear outliers and no additional outliers are left.

Our fitted three-harmonics model is shown in red in Figure 7, including residuals in the bottom panel, and the fitted amplitudes listed in Table 5 bottom part. The fitted two-harmonics model is shown in blue in Figure 7 and the fitted coefficients listed in Table 5 upper part. The fitted values were derived using a linear least squares method, while the error bars were determined using the prayer bead approach. The median of those distributions was identical to the originally fitted values. To test our results, we repeated the analysis for each quarter separately and then took the average between all quarters. The results of this "quarter averaging" approach were indistinguishable from our original results.

Table 5 lists the measured amplitudes in the middle column and also the corrected amplitudes, after multiplying by the

Kepler dilution factor (see Section 2.6 and Table 9), in the right-most column. The errors on the latter account for the errors in both the measured amplitudes and the dilution factor. Comparing the fitted amplitudes between the two models shows that adding an additional harmonic component in the three-harmonics model does not change the amplitudes significantly, albeit perhaps the reflection amplitude where the corrected amplitude increased by 1.6σ, which is equivalent to an increase of 2.2%.

The Figure 7 bottom panel shows that the two-harmonics model residuals have significant systematic features that do not appear in the three-harmonics model residuals, indicating that the latter is a more complete model than the former. Adding additional higher harmonics to the model does not result in statistically significant fitted amplitudes. Although a_{3c} and a_{3s} are small, at the level of several parts per million, they are statistically significant. This signal, at one-third the orbital period, was already identified by Esteves et al. (2013) with a consistent amplitude.[26] It is at least partially due to a higher order component of the tidal ellipsoidal distortion (Morris 1985; Morris & Naftilan 1993), although the theoretically predicted amplitude is about half the overall amplitude of the measured signal at one-third the orbital period and has a different phase, so there is an additional process or processes in play here. This could be related to an incomplete understanding of tidal ellipsoidal modulations of massive stars with radiative envelopes, especially when the stellar spin axis is not aligned with the orbital angular momentum axis and the stellar rotation rate is not synchronized with the orbit (Pfahl et al. 2008; van Kerkwijk et al. 2010; Jackson et al. 2012), as is the case for Kepler-13A. Another possibility is that this signal originates from a more complicated planetary surface distribution pattern than assumed here (Cowan et al. 2013). A detailed investigation of the combination of these effects is beyond the scope of this study.

The parameters we fitted in Shporer et al. (2011) are $\leqslant 2\sigma$ of the values derived here. Differences could arise from the changes in our analysis method. Here we used the highly precise occultation ephemeris, whereas in Shporer et al. (2011), we used an ephemeris derived from analysis of the photometric orbital modulations themselves. In Shporer et al. (2011), we also did not remove instrumental trends by fitting cotrending basis vectors.

2.5.1. Planetary Mass Estimate

The beaming and ellipsoidal phase modulation amplitudes depend linearly on the planetary mass, so the latter can be estimated using the corrected amplitudes (Table 5 rightmost column), $A_{\rm beam}$ and $A_{\rm ellip}$, along with other parameters of the system and the host star:

$$M_{\rm p,\,beam}\sin i = \frac{0.37}{\alpha_{\rm beam}}\left(\frac{M_{\rm s}}{M_{\odot}}\right)^{2/3}\left(\frac{P_{\rm orb}}{\rm day}\right)^{1/3}\left(\frac{A_{\rm beam}}{\rm ppm}\right) M_{\rm J}, \quad (12)$$

$$M_{\rm p,\,ellip}\sin i = \frac{0.077}{\alpha_{\rm ellip}\sin i}\left(\frac{R_{\rm s}}{R_{\odot}}\right)^{-3}\left(\frac{M_{\rm s}}{M_{\odot}}\right)^{2} \times \left(\frac{P_{\rm orb}}{\rm day}\right)^{2}\left(\frac{A_{\rm ellip}}{\rm ppm}\right) M_{\rm J}, \quad (13)$$

[26] We corrected the amplitude reported by Esteves et al. (2013) to account for the weaker dilution assumed by those authors.

Table 6
Companion Mass Estimates

Method	Value
$M_{\rm p,beam}\sin i$, $M_{\rm J}$	7.57 ± 0.52
$M_{\rm p,ellip}\sin i$, $M_{\rm J}$	5.94 ± 1.00

where $M_{\rm s}$ and $R_{\rm s}$ are the host mass and radius, P and i are the orbital period and orbital inclination angle, and $\alpha_{\rm beam}$ and $\alpha_{\rm ellip}$ are order of unity coefficients. We note that $\sin i$ can be ignored because as measured by Barnes et al. (2011) it is close to unity, as expected for this transiting system.

The beaming coefficient, which accounts for the photons being Doppler shifted in and out of the observed bandwidth along the orbital motion of the star, is calculated as

$$\alpha_{\rm beam} = \frac{x e^{x}}{e^{x}-1} = 0.80 \pm 0.02, \left(x \equiv \frac{h\nu}{k_{\rm B} T_{\rm eff}}\right), \quad (14)$$

where h is Planck's constant, ν the observed frequency, k_B the Boltzman constant, and $T_{\rm eff}$ the host star's effective temperature. For the latter we used the value derived here while integrating over the *Kepler* transmission curve.[27] The error reported above accounts for the error in $T_{\rm eff}$.

The ellipsoidal coefficient is approximated as (Morris & Naftilan 1993)

$$\alpha_{\rm ellip} = 0.15\frac{(15+u)(1+g)}{3-u} = 1.43 \pm 0.14, \quad (15)$$

where u is the stellar limb-darkening coefficient assuming a linear limb-darkening law, and g is the gravity-darkening coefficient. We estimated those coefficients using the grids of Claret & Bloemen (2011) and stellar parameters derived here.

Equations (12) and (13) assume that the companion is a nonluminous object, so the observed beaming and ellipsoidal modulations are entirely due to the host star's motion, not the planetary companion. This assumption is not entirely correct because the planet does have a measurable contribution to the total flux in the optical. This contribution is at the 10^{-4} level (Section 2.4), and less during the transit phase (Section 3.1), so its contribution to the measured amplitudes is less than the amplitude errors even when accounting for the planetary companion's larger RV amplitude (Zucker et al. 2007; Shporer et al. 2010).

Our derived planetary masses using the beaming and ellipsoidal modulations amplitude are listed in Table 6, where the errors account for the errors on all parameters in the right-hand side of Equations (12) and (13), leading to significantly larger fractional errors for the mass estimates than for the beaming and ellipsoidal corrected amplitudes (see Table 5). The two estimates are 1.8σ from each other[28] and differ by a factor of 1.27 ± 0.23. Similar discrepancies were reported by other authors for other systems (e.g., van Kerkwijk et al. 2010; Carter et al. 2011; Bloemen et al. 2012; Barclay et al. 2012; Faigler et al. 2013; Esteves et al. 2013) and for this system by Mazeh et al. (2012) using only two quarters of *Kepler* long-cadence data. The reason for this discrepancy is currently not clear. One possibility is inaccurate stellar parameters, meaning a poor understanding of

[27] http://keplergo.arc.nasa.gov/CalibrationResponse.shtml

[28] The statistical significance of the difference between the two mass estimates was calculated while accounting for the fact that they are *not* independent. For example, they are both derived using the same stellar mass and dilution factor.

the nature of the host star, which is more probable for early-type stars where accurate stellar parameters (e.g., mass, gravity, temperature) are difficult to obtain compared to Sun-like stars. The refined stellar parameters and dilution factor obtained here result in a smaller beaming-based planet mass estimate compared to our results in Shporer et al. (2011).

Another possibility for the origin of the discrepancy is a poor understanding of the ellipsoidal effect for hot stars such as Kepler-13A (Pfahl et al. 2008; van Kerkwijk et al. 2010). Further reason to doubt the ellipsoidal mass estimate comes from Ehrenreich et al. (2011) and Bloemen et al. (2012), who measured the RV amplitude of the A-type primary in KOI-74 and showed that it agreed with the beaming amplitude and did not agree with the ellipsoidal amplitude (van Kerkwijk et al. 2010; Bloemen et al. 2012). However, one should be careful when comparing Kepler-13 and KOI-74. The A-type primary in KOI-74 is almost 2,000 K hotter than Kepler-13A and the secondary is not a planet but a white dwarf (van Kerkwijk et al. 2010; Ehrenreich et al. 2011; Bloemen et al. 2012), leading to observed photometric amplitudes a few orders of magnitude larger. On the other hand, some authors have reported cases where the known RV amplitudes were consistent with the ellipsoidal-based mass estimate and inconsistent with the beaming-based mass estimate (e.g., Faigler et al. 2013; Esteves et al. 2013). However, all of the latter cases involve convective Sun-like stars.

We therefore take a conservative approach and conclude that our planet mass estimate lies within the range of 4.94–8.09 M_J with a 1σ confidence. This estimate, derived using the refined stellar parameters and dilution factor obtained here, is consistent with previous estimates (Shporer et al. 2011; Mazeh et al. 2012; Mislis & Hodgkin 2012; Esteves et al. 2013; Placek et al. 2013), confirming that this planet belongs to the rare class of massive hot Jupiters. The A-type nature of the host star might represent an extension of the tendency of hot Jupiters at this mass range and above, into the brown dwarf mass range, to orbit F-type stars as opposed to G-type Sun-like convective stars (Bouchy et al. 2011a, 2011b).

2.6. Spectroscopic Analysis

As we have already noted, because the two A-type stars are at a separation of $1''.15 \pm 0''.05$ (see Figure 1 and Section 1.1), they are fully blended in all of our photometric data sets. A correct astrophysical interpretation of any measured photometric variability requires an estimate of the "real" variability amplitude that would have been measured if the star was resolved. Obtaining those amplitudes from the directly measured ones requires knowledge of the flux ratio between the two stars in the observed bands. We estimate the magnitude of this dilution using two high-resolution spectra of the two stars, taken with the Keck/HIRES spectrograph (Vogt et al. 1994) on UT 2010 June 3. The spectra were taken while placing the slit perpendicular to the position angle between the two stars. Given the slit width of $0''.86$ and the typical $0''.5$ astronomical seeing at the Keck Observatory, we estimate that the contamination between the two spectra is no more than 10%, and we did not see any signs of contamination in our visual examination of the raw spectra.

According to Santerne et al. (2012), the third star in the system, Kepler-13BB, contributes very little to the overall system luminosity, from approximately 1% in the optical to 2% in the IR. We therefore ignore its existence in the following analysis and treat the system as consisting of two A-type stars.

The spectra of components A and B were fitted individually to derive precise stellar parameters and to predict the flux ratio between the two components throughout a wide range of wavelengths, from the optical to the IR. In this step, we made use of the Phoenix spectral models (Hauschildt et al. 1999; Husser et al. 2013) and followed the fitting recipe described in Szabó et al. (2011). Unfortunately, the rapid rotation of both stars meant that the metal lines were blended, resulting in degeneracies in our retrieved stellar parameters. The temperatures of the two components were determined to be 7,650 K and 7,530 K, with 250 K errors for both values. Although the χ^2 surface of the fit in the $T_{\rm eff}$ – $\log g$ grid was wide with a shallow bottom, the error surfaces could have been shifted to each other with a temperature shift of 120 ± 50 K. This means that the spectra better constrained the temperature difference than the individual temperatures. A temperature difference of 120 ± 50 K is also consistent with the results of Szabó et al. (2011) from optical photometric colors.

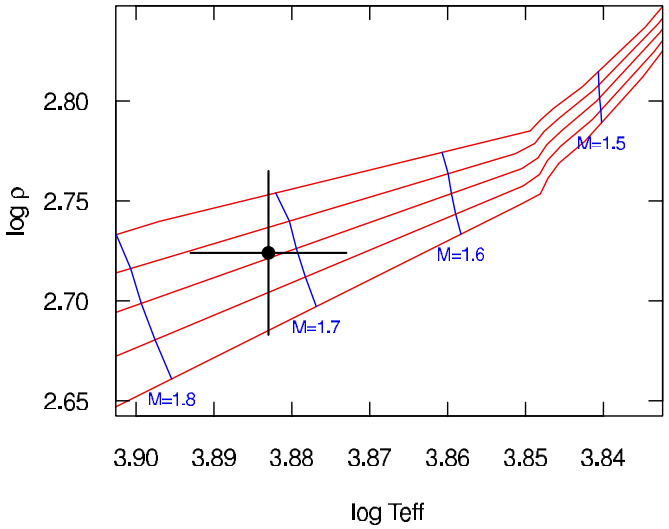

Figure 8. Position of Kepler-13A (black circle and 3σ error bars) in the density (in kg m^{-3}) vs. effective temperature diagram. Red lines are Padova isochrones in steps of 100 Myr, from 300 Myr at the top to 700 Myr at the bottom, and blue lines are equal stellar mass lines (see labels).

(A color version of this figure is available in the online journal.)

To improve the fits, we assumed that the two stars have identical ages and metallicities and used the average density of Kepler-13A determined from the transit light curve (e.g., Winn 2011). Because the geometry of the Kepler-13Ab orbit is known and the transit chord is precisely determined (Barnes et al. 2011), the transit duration constrains the density of the host star. Following the recipe of Winn (2011), the derived density of Kepler-13A is 0.53 ± 0.01 g cm^{-3}, 0.37 times the solar value. The 2% error is mostly due to the uncertainty in the impact parameter.

Knowing the temperature and density of Kepler-13A, we can plot its position on the appropriate density–temperature isochrones. Stellar models were taken from the Padova isochrone family with [Fe/H] = 0.2 metallicity (Bertelli et al. 2008, 2009). We find a good fit to the 0.5 Gyr old isochrones, whereas the 0.4 and 0.6 Gyr models were beyond the 1σ error, as shown in Figure 8 where we plot the 3σ errorbars. Our results therefore point to a 0.5 ± 0.1 Gyr age for the Kepler-13 system, consistent with Szabó et al. (2011). Stellar parameters are listed in Table 7.

The final step was to simulate the spectra of stars with masses, radii, and temperatures as indicated in Table 7, assuming $v \sin i = 65$ km s^{-1} (Szabó et al. 2011). For this we used

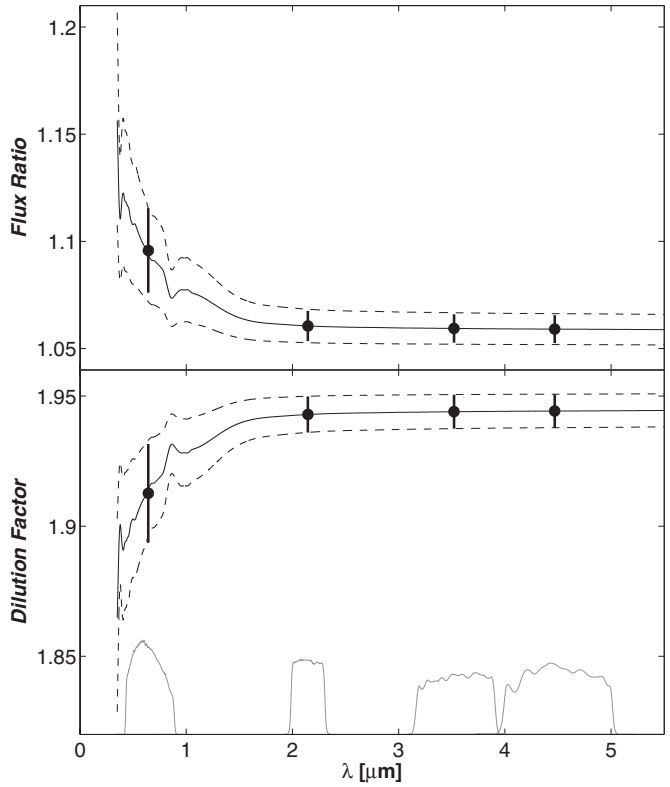

Figure 9. Top: flux ratio between the planet-hosting star Kepler-13A to its binary companion Kepler-13B, as a function of wavelength. Bottom: the multiplicative factor that corrects the measured variability amplitude (occultation depths and sinusoidal variability) to account for the dilution of the two stars, as a function of wavelength. In both panels, curves were smoothed using iterative Savitzky–Golay smoothing for presentation purposes. Dashed lines represent the 1σ uncertainties, and filled circles with error bars are the values integrated over the bandpasses of our observations. These bandpasses are shown at the bottom of the figure, with an arbitrary Y-axis scale for presentation purposes.

Table 7
Stellar Parameters

Parameter	Kepler-13A	Kepler-13B
$T_{\rm eff}$, K	$7{,}650 \pm 250$	$7{,}530 \pm 250$
$\log(g\ [\mathrm{g\ cm^{-2}}])$	4.2 ± 0.5	4.2 ± 0.5
[Fe/H]	0.2 ± 0.2	0.2 ± 0.2
$V_{\rm rot}$, km s^{-1}	78 ± 15	69 ± 13
Age, Gyr	0.5 ± 0.1	0.5 ± 0.1
Mass, $M_\odot$	1.72 ± 0.10	1.68 ± 0.10
Radius, $R_\odot$	1.71 ± 0.04	1.68 ± 0.04

Phoenix models scaled by the areas of the stellar disks and interpolated to temperatures of 7,650 K and 7,530 K. This way the flux ratios were determined for a wide wavelength range with high resolution, plotted in Figure 9 and listed in Table 8. We calculated the flux ratio for each band as the weighted average of the flux ratio across the relevant wavelength range using the known transmission curves as weights. Table 9 lists the dilution factorthe factor by which each occultation depth needs to be multiplied to correct for the dilutionfor each of the four bands used here.

We note that using the revised planet host star's radius derived here and the planet-to-star radii ratio from Barnes et al. (2011) we obtain a revised planet radius of $R_p = 1.406 \pm 0.038\ R_{\rm J}$. We also use the revised planet host star parameters in deriving the planet's mass in Section 2.5.1.

Table 8
Kepler-13A / Kepler-13B Flux Ratio

Wavelength (Å)	Flux Ratio	Upper Limit	Lower Limit
3500.087	1.148113	1.194621	1.102890
3500.239	1.149844	1.197161	1.103864
3500.391	1.150445	1.198042	1.104202
3500.543	1.150080	1.197507	1.103997
3500.695	1.149214	1.196236	1.103509
3500.848	1.148232	1.194795	1.102956
3501.000	1.147166	1.193231	1.102356
3501.152	1.145494	1.190779	1.101415
3501.304	1.143709	1.188160	1.100410
3501.457	1.142740	1.186738	1.099864

Notes. Columns include, from left to right: wavelength, flux ratio, flux ratio 1σ upper boundary, and flux ratio 1σ lower boundary.

(This table is available in its entirety in a machine-readable form in the online journal. A portion is shown here for guidance regarding its form and content.)

3. ATMOSPHERIC CHARACTERIZATION

We studied the atmosphere using two different approaches. In the first (Section 3.1), we used a highly simplistic model where the small number of parameters allowed us to fit them despite the small number of data points. In the second (Section 3.2), we used models with many parameters, so we could not fit the models to our data but only do a qualitative comparison.

3.1. Energy Budget

The day-side luminosity is a combination of thermal emission and reflected stellar light. Therefore it depends on the day-side brightness temperature, $T_{\rm D}$, and geometric albedo, $A_{\rm g}$, in the corresponding wavelength. The expected occultation depth, D, in relative flux, is the ratio between the planet's day-side luminosity and the star's flux and is a function of three variables:

$$D(\lambda, T_{\rm D}, A_{\rm g}) = \left(\frac{R_p}{R_s}\right)^2 \frac{B_p(\lambda, T_{\rm D})}{I_s(\lambda)} + A_{\rm g}\left(\frac{R_p}{a}\right)^2, \quad (16)$$

where we take the planet's day-side emission spectrum, B_p, to be a blackbody spectrum so it depends only on wavelength, λ, and $T_{\rm D}$. We use a Phoenix stellar atmosphere model for the star's spectrum (I_s) interpolated to match the $T_{\rm eff}$ and $\log g$ from Table 7. Because the geometric parameters of the system (R_p/R_s, a/R_s) are known, the expected occultation depth at a given wavelength depends on two variables, $T_{\rm D}$ and $A_{\rm g}$. In Figure 10, we plot the relation between these two variables for each of the observed bands, including the 1σ region while marginalizing over all of the parameters in Equation (16). We exclude the WIRC/K_s occultation measurement in Figure 10 because in that measurement's low S/N, the corresponding 1σ region encompasses both those of the IRAC/3.6 μm and IRAC/4.5 μm regions, so it does not add any information. The $A_{\rm g}$–$T_{\rm D}$ relation for the *Kepler* band goes from two extreme scenarios: a cold atmosphere with a high geometric albedo where the day-side luminosity is dominated by reflected stellar light on one end, and a hot atmosphere with a negligible albedo where the day-side luminosity is dominated by thermal emission on the other end. The almost vertical shape of the $A_{\rm g}$–$T_{\rm D}$ curves for the two *Spitzer* bands means that in the IR the day-side luminosity is dominated by thermal emission and depends only weakly on the geometric albedo.

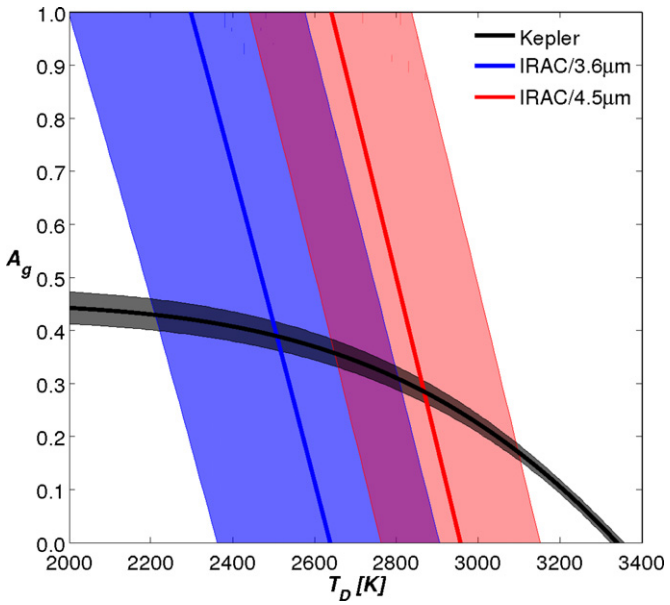

Figure 10. Geometric albedo vs. day-side brightness temperature for three of the observed bands, *Kepler* in black, IRAC/3.6 μm in blue, and IRAC/4.5 μm in red. The solid lines are calculated according to Equation (16) and the measured occultation depths, and the filled regions are the corresponding 1σ uncertainty while marginalizing over the parameters in Equation (16). The area where the IRAC/3.6 μm and IRAC/4.5 μm 1σ regions overlap is marked in purple. The WIRC/K_s band occultation measurement is ignored here because its low S/N results in a wide 1σ region that encompasses both those of the IRAC/3.6 μm and IRAC/4.5 μm so it does not add information.

(A color version of this figure is available in the online journal.)

None of the four bands in which we observed the occultation is at the peak of the blackbody spectrum for a body with an effective temperature similar to that of Kepler-13Ab atmosphere.[29] However, the four bands sample both sides of the peak: Wien's tail in the optical and the Rayleigh–Jeans tail in the IR. Therefore it is interesting to check if the same day-side brightness temperature can reproduce all four measured occultation depths because that will give an estimate of the equivalent of the day-side *effective* temperature, $T_{\rm D,eff}$. We do not need to assume here that the day-side atmosphere behaves as a black body. By definition $T_{\rm D,eff}$ is the effective temperature of a black body that shows the same occultation depths in the four wide bands we measured. We do need to assume, however, that $A_{\rm g}$ remains the same across the observed bands because this requires simultaneously fitting $T_{\rm D,eff}$ and $A_{\rm g}$ to all four occultation depths, using Equation (16). Visually, the allowed values correspond to the overlap region in Figure 10. Fitting using a dense two-dimensional grid results in $T_{\rm D,eff} = 2750 \pm 160$ K and $A_{\rm g} = 0.33^{+0.04}_{-0.06}$, where the two variables are highly correlated. Although formally we assumed here that $A_{\rm g}$ is the same across the wavelength range we observed in, in practice because in the IR $T_{\rm D}$ depends weakly on $A_{\rm g}$ the above result for $T_{\rm D,eff}$ will change only in case of a large variation in $A_{\rm g}$ from the optical to the IR. Assuming a brightness temperature equal to the derived $T_{\rm D,eff}$, varying $A_{\rm g}$ from 0.0 to 0.5 will change the IRAC/3.6 μm occultation depth by no more than 1σ, while the corresponding $A_{\rm g}$ range for the IRAC/4.5 μm band is from 0.0 to 1.0. Meaning, $A_{\rm g}$ is constrained primarily by the occultation depth in the optical.

[29] According to Wien's displacement law, for effective temperatures in the range of 2500 K to 3000 K, the blackbody spectrum peaks at 1.16 μm to 0.97 μm.

3.2. Detailed Atmospheric Modeling

In Figure 11 we compare the occultation depths measured here to the expected occultation depth as a function of wavelength from detailed atmospheric models. The left panel in Figure 11 shows two models based on Fortney et al. (2008) using a one-dimensional, plane-parallel atmosphere code and assuming local thermodynamic equilibrium (LTE) and solar composition. The two models shown both assume even heat distribution across the day side and no recirculation to the night side, parameterized by Fortney et al. (2008) as $f = 0.5$. In one model, TiO is added in equilibrium abundances to the upper atmosphere, where it acts as an absorber that induces a high-altitude temperature inversion. In the second model, TiO is excluded because this species may be depleted because of cold traps on the night

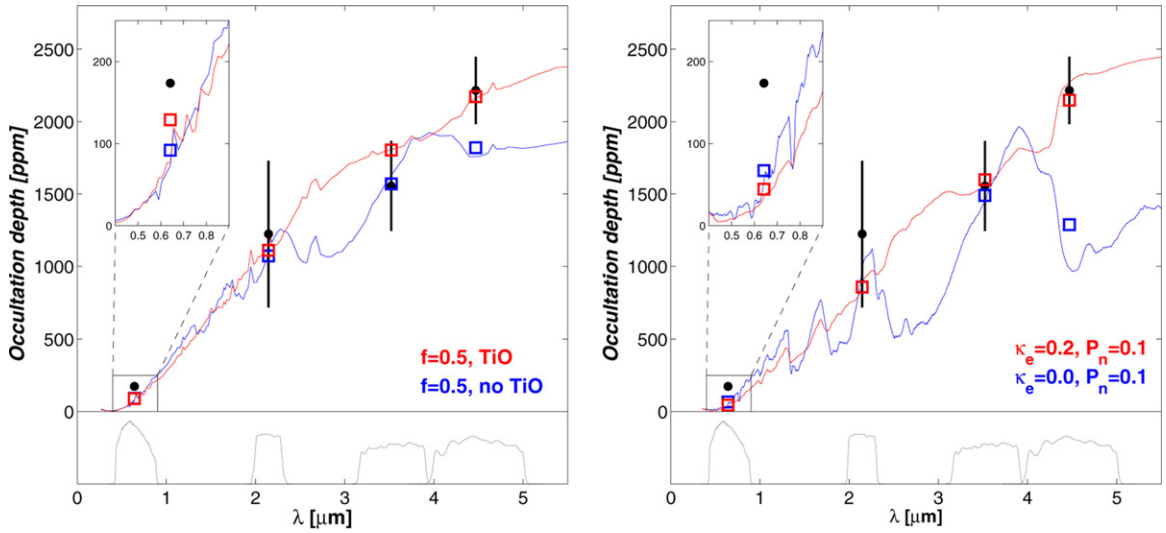

Figure 11. Occultation depth vs. wavelength for Kepler-13Ab, showing atmospheric models (solid lines, color coded) for different parameterizations (see legend). Occultation depths measured here are marked in black. Transmission curve of each band is plotted in gray at the bottom. The inset shows a zoom-in on the *Kepler* wavelength region, while the error bar on *Kepler* occultation depth is too small to be seen in this scale. Left panel shows models based on Fortney et al. (2008), and the right panel is based on models of Burrows et al. (2008).

(A color version of this figure is available in the online journal.)

Table 9
Occultation Depths and Light Curve Scatter

Band	Scatter (%)	PNR (% min)	Measured Depth (%)	Dilution Factor	Corrected Depth (%)
IRAC/4.5 μm	0.339	0.141	0.114 ± 0.012	1.9442 ± 0.0064	0.222 ± 0.023
IRAC/3.6 μm	0.442	0.105	0.080 ± 0.016	1.9440 ± 0.0065	0.156 ± 0.031
WIRC/K_s	0.360	0.206	0.063 ± 0.026	1.9429 ± 0.0070	0.122 ± 0.051
Kepler	0.0109[a]	0.00050[b]	0.009081 ± 0.000027	1.913 ± 0.019	0.01737 ± 0.00018

Notes.
[a] Scatter (MAD) in the unbinned short-cadence light curve.
[b] PNR (photometric noise rate) of the phase-folded and binned light curve, using 1 minute bins.

side and in the deep interior. We also consider models from Burrows et al. (2008), who similarly assume a plane-parallel atmosphere, LTE, and solar composition and use the opacity calculations of Sharp & Burrows (2007). Those are shown in the right panel of Figure 11 and are parameterized by κ_e, an absorption coefficient of a gray absorber in the stratosphere, and P_n, an energy redistribution coefficient, ranging from 0.0 for redistribution across the day side only to 0.5 for redistribution across the day and night hemispheres.

Comparing the two sets of models with our measured occultation depths shows that the inverted models are more consistent with the data than the noninverted models, although that is based only on the 4.5 μm point. An inverted atmosphere for Kepler-13Ab is consistent with the trend identified by Knutson et al. (2010), that planets orbiting chromospherically quiet stars tend to have inverted atmospheres. Although it is a different proxy for stellar activity, the *Kepler* light curve shows an especially quiet star, and apart from variability induced by the orbiting planetary companion (Section 2.5), the light curve shows only a $\sim$10 ppm sinusoidal variability at a period of 1.06 days (Shporer et al. 2011; Szabó et al. 2011; Mazeh et al. 2012). That low-level variability could be due to stellar activity but may also be due to stellar pulsations. It is also possible that it originates from the Kepler-13B system as the light from all stars in the system is fully blended in the *Kepler* light curve.

The correlation identified by Hartman (2010), between increased planetary surface gravity and increased host-star chromospheric activity, is not supported by the Kepler-13A system because the planet has a high surface gravity and the host star shows low-level variability in the light curve. Although, we note that both the Knutson et al. (2010) and Hartman (2010) correlations were identified only for Sun-like convective stars, not for early-type stars like Kepler-13A.

3.3. Night-Side Optical Luminosity

The *Kepler* measurements of both the occultation depth and reflection modulation amplitude allow us to measure the planet's night-side optical luminosity. The occultation depth measures the luminosity of the day-side hemisphere, while the reflection amplitude measures the difference between the day and night hemisphere luminosities. The difference between the occultation depth and reflection (full) amplitude gives the night-side luminosity:

$$\Delta_{\rm NS} = \Delta_{\rm DS} - 2 \times A_{\rm ref} = 17.36 \pm 1.48 \ \ {\rm ppm}, \qquad (17)$$

where $\Delta_{\rm NS}$ is the night-side luminosity and $\Delta_{\rm DS}$ the day-side luminosity. The result presented in Equation (17) is corrected for the dilution in the *Kepler* band (see Table 9). This detection of the night-side optical luminosity is beyond 11σ and is consistent with previous estimates (Mazeh et al. 2012; Esteves et al. 2013).

Next we derive the planet's night-side brightness temperature, $T_{\rm N}$, using the above night-side optical luminosity, the host star's parameters (see Table 7), the planet-to-star radii ratio (see Table 4), and *Kepler* 's transmission curve. We assumed a blackbody spectrum for the planet and used Phoenix stellar synthetic spectra (Husser et al. 2013) for the star, while marginalizing across the grid points close to the star's $T_{\rm eff}$ and $\log g$, resulting in $T_{\rm N} = 2537 \pm 45$ K. Using a blackbody spectrum for the star gives the same $T_{\rm N}$.

While $T_{\rm N}$ is smaller than $T_{\rm D,eff}$ derived above, the difference is not large. Assuming that the night-side effective temperature equals the night-side brightness temperature as measured in the *Kepler* band, we can use the formalism of Cowan & Agol (2011, see their Equations (4) and (5)) to constrain the day-side to night-side heat redistribution coefficient ε together with the bond albedo $A_{\rm B}$. Using that formalism, we get a heat redistribution coefficient of $\varepsilon = 0.88 \pm 0.10$ and bond albedo $A_{\rm B} \leqslant 0.14$ at 1σ. The high ε indicates an efficient heat redistribution process, although the low $A_{\rm B}$ is inconsistent with the high $A_{\rm g}$ derived above assuming $A_{\rm B} = (3/2)A_{\rm g}$ (Lamert's Law), which results in $A_{\rm B} = 0.50^{+0.06}_{-0.09}$. On the other hand, assuming the latter value for $A_{\rm B}$ requires $\varepsilon > 1$ in order to reach the derived $T_{\rm N}$. This shows that the night-side brightness temperature, measured only in the optical, is not a good proxy for the night-side effective temperature, meaning that the night side does not behave like a black body in the optical. Yet, a high ε cannot be ruled out here.

3.4. Comparison with WASP-33b

It is interesting to compare Kepler-13Ab to WASP-33b (Collier Cameron et al. 2010; Kovács et al. 2013) because these are currently the only two known transiting hot Jupiters orbiting bright A-type stars. The planets in both systems orbit similar stars, have orbital periods in the one to two days range, have consistent (at the 1σ level) equilibrium temperatures, and experience consistent incident flux at the planet surface. Both systems also have orbits that are misaligned with the host stars' spin axes (Collier Cameron et al. 2010; Barnes et al. 2011), suggesting a similar orbital evolution scenario. WASP-33 may also be part of a binary star system (Moya et al. 2011), although its smaller and cooler candidate companion has not been confirmed with common proper motion measurements. WASP-33b has a mass of $3.266 \pm 0.726\ M_{\rm J}$ and a radius of $1.679^{+0.019}_{-0.030}$ $R_{\rm J}$ (Kovács et al. 2013). Its smaller mass and slightly larger radius than Kepler-13Ab leads to a mean density 3–4 times smaller, and a surface gravity ($\log_{10} g$) 0.3–0.5 smaller.

Occultations of WASP-33b have been observed in the *Spitzer* IRAC/3.6 μm and IRAC/4.5 μm bands (Deming et al. 2012), the K_s band (Deming et al. 2012; de Mooij et al. 2013), and a narrow-band S[III] filter at 0.91 μm (Smith et al. 2011). In this

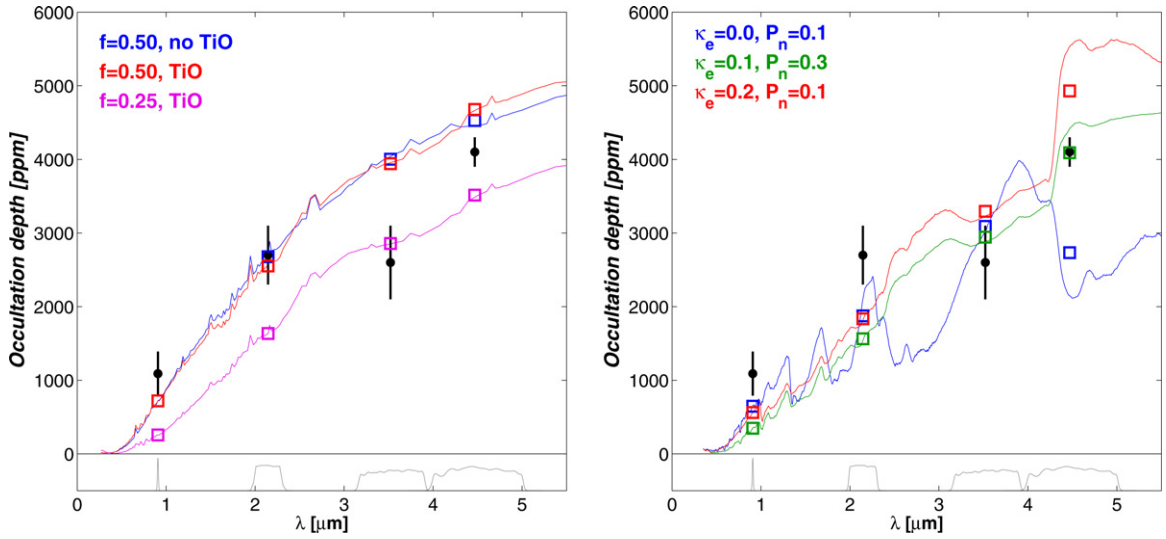

Figure 12. Occultation depth vs. wavelength for WASP-33b, showing atmospheric models (solid lines, color coded) for different parameterizations (see legend). Occultation depths from the literature are marked in black. Transmission curve of each band is plotted in gray at the bottom. Left panel shows models based on Fortney et al. (2008), and the right panel is based on models of Burrows et al. (2008).

(A color version of this figure is available in the online journal.)

case measurements of the occultation depth are hampered by the host star's δ-Scuti pulsations, measured in the *R* band by Herrero et al. (2011) to have a primary modulation component at 1.1 hr with an amplitude of 0.1% (see also von Essen et al. 2014), seen also in the IR (Deming et al. 2012). These pulsations can bias estimates of the WASP-33b occultation light curve shape, especially when based on a single occultation event that is 2.8 hr long and its depth ranges from 0.4% at 4.5 μm down to 0.1% at 0.91 μm.

To compare the atmospheres of the two planets, we have calculated the WASP-33b atmospheric models corresponding to those plotted in Figure 11 for Kepler-13Ab and plotted them in Figure 12 along with additional models with different parameters. The figure shows that none of the models are consistent with all four measured occultation depths, although the data appear to be closest to models with moderate to weak day–night recirculation and a modest temperature inversion. In this case it is possible that the discrepancies between the models and the measured occultation depths are the result of biases introduced by the δ-Scuti pulsations of the host star; our group will test this in the near future with full-orbit *Spitzer* phase curve observations including two occultations in both the IRAC/3.6 μm and IRAC/4.5 μm bands. Deming et al. (2012) explored fitting the WASP-33b occultation depths with the models of Madhusudhan & Seager (2009, 2010), which allow the relative abundances of water, methane, CO, and CO_2 as well as the vertical pressure–temperature profile to vary as free parameters in the fit. They find that their models generally prefer inefficient day–night recirculation, and in the case of solar metallicity composition they prefer a day-side temperature inversion. They also identify a family of models that match the data without a temperature inversion and with a supersolar C-to-O ratio, shown by Madhusudhan (2012) to fit the data marginally better.

4. DISCUSSION AND CONCLUSIONS

We present here a multiband study of the atmosphere of Kepler-13Ab. We measured the occultation depth of Kepler-13Ab in four wide bands, from the IR (*Spitzer*/IRAC 4.5 μm and 3.6 μm) through the NIR (P200/WIRC/K_s) to the optical (*Kepler*). We also used *Kepler* data along the entire orbit to measure the planetary reflected and thermally emitted light and measure the planetary mass from the beaming and ellipsoidal effects. Finally, we used Keck/HIRES spectroscopic data to characterize the planet host star and calculate the dilution of the observed occultations due to the presence of a blended A-type companion star. The measured occultation depths are listed in Table 9 including both the directly measured depths, not accounting for the dilution, and the corrected depths while accounting for the dilution. The corrected depths are simply the measured depths multiplied by the dilution factor at the respective wavelength, also listed in Table 9. The corrected depth uncertainties account for both the measured depth uncertainties and dilution factor uncertainties.

Comparing the *Kepler* midoccultation time derived here (see Table 4 and Section 2.4) to the midtransit time from the literature shows that the midoccultation time occurs about half a minute earlier, with a significance of almost 5σ (Section 2.4.1). This can be attributed to either a nonzero orbital eccentricity or an asymmetric distortion in the light curve ingress and egress shape due to asymmetric planetary surface brightness distribution, meaning the brightest region on the planet's surface is shifted away from the substellar point. An early midoccultation time can be the result of superrotating winds causing the planet's most reflective region to be shifted westward, as already identified for Kepler-7b by Demory et al. (2013). Interestingly, Kepler-7b's high geometric albedo and day-side brightness temperature in the optical (Demory et al. 2011; Kipping & Bakos 2011), as well as the planet and host star radii (Latham et al. 2010), are all comparable to those of Kepler-13Ab. However, Kepler-7b's mass is only $0.433 \pm 0.040\ M_J$, more than ten time less massive than the Kepler-13Ab mass, and its host star has a mass of about 1.35 $M_\odot$ and effective temperature of about 6000 K (Latham et al. 2010).

By analyzing the *Kepler* phase curve we have identified a discrepancy between the beaming-based and ellipsoidal-based planet's mass estimates (see Table 6 and Section 2.5.1), which was already noticed before (Shporer et al. 2011; Mazeh et al. 2012). We chose to take a conservative approach and give a wide range for the planet's mass that includes both estimates.

If the early mid-occultation time is indeed due to the brightest region of the planetary atmosphere being shifted away from the substellar point, then that may also affect the observed phase curve. Specifically, that will insert a phase shift to the reflection component in Equation (11), which includes both thermal emission and reflected stellar light from the planet's atmosphere. In that case the measured coefficients a_{1c} and a_{1s} would not correspond separately to the reflection and beaming amplitudes but to a linear combination of them, meaning the model will include a degeneracy. This was already noted by Faigler et al. (2013), who analyzed the phase curve of Kepler-76b. Although the host star in that system is an F-star, so it is different than the host star in the Kepler-13A system, they have shown that adding a phase shift to the reflection component results in a decreased beaming-based mass estimate for Kepler-76b and makes it consistent with the ellipsoidal-based mass estimate. Following a similar scheme (see Faigler et al. 2013, Equation (1)), the required phase shift of the reflection component that will resolve the corresponding discrepancy for Kepler-13Ab (see Table 6) is 1.49 ± 0.48 deg. However, such a phase shift will put the planet's brightest region eastward of the substellar point, so the resulting asymmetry in the occultation light curve ingress and egress will make the midoccultation time later than expected, not earlier as we measure here. We conclude that if the measured early midoccultation time is due to a planetary asymmetric surface brightness distribution we cannot detect direct evidence for it in the phase curve.

Our revised host star parameters show it is smaller than previous estimates (Szabó et al. 2011), leading to a smaller planetary radius of $R_p = 1.406 \pm 0.038\ R_J$ where we assume the planet-to-star radii ratio reported by Barnes et al. (2011). This revised planet radius is comparable with the radii of other hot Jupiters, although given the planet's relatively high mass it is positioned in a sparse region in the planetary radius-mass diagram for the currently known planets.

We have followed two approaches for interpreting our measurements and characterizing Kepler-13Ab's atmosphere. In Section 3.1, we study the atmospheric energy budget, and in Section 3.2, we compare our wide-band measurements to various spectral atmospheric models. We must caution here that our conclusions about Kepler-13Ab's atmosphere are based on sparse data. Although covering a wide wavelength range, from the IR to the optical, we have at hand the occultation depth measured in only four wide bands and the phase curve measured in only one wide band. Such sparse data could, in principle, lead to systematically biased results when fitted with over-simplified atmospheric models (see Burrows 2013 for a more detailed discussion). Despite the limited data, our analysis here, including the two different approaches (Sections 3.1 and 3.2), is an attempt to extract as much science as possible from the data while not over-interpreting it. In the future, more detailed data, including panchromatic spectra and phase curves at various wavelengths, will allow a more comprehensive characterization of the planet's atmosphere.

The four occultation measurements enable us to identify the relation between the day-side brightness temperature and geometric albedo in each band (see Equation (16) and Figure 10). Assuming the geometric albedo does not change significantly between the four bands, these relations allow us to derive the effective temperature of a black body that will show the same occultation depths, $T_{\rm D,eff} = 2750 \pm 160$ K. This also results in a high geometric albedo, of $A_g = 0.33^{+0.04}_{-0.06}$, which assuming $A_B = (3/2)A_g$ (Lambert's Law) leads to $A_B = 0.50^{+0.06}_{-0.09}$. Such an albedo is at the high end of the range spanned by other hot Jupiters (e.g., Rowe et al. 2008; Cowan & Agol 2011; Coughlin & López-Morales 2012; Evans et al. 2013; Demory et al. 2013; Heng & Demory 2013).

The night-side brightness temperature in the optical is $T_N = 2537 \pm 45$ K, measured from the difference between the *Kepler* occultation depth and the reflection component amplitude (see Equation (17)). T_N is smaller than $T_{\rm D,eff}$ but not by much. Comparing T_N, $T_{\rm D,eff}$, and A_B results in inconsistencies, indicating that the night side does not behave as a black body in the optical.

A possible explanation for the small difference between T_N and $T_{\rm D,eff}$ is the planet's high mass, from at least five to nearly ten times larger than that of typical hot Jupiters, which gives a correspondingly large surface gravity with $\log_{10}(g\ [\mathrm{g\ cm^{-2}}])$ in the range of 3.79–4.01. Increased gravity leads to increased photospheric pressure, which in turn increases the radiative time constant in the atmospheric layers probed by our measurements (Iro et al. 2005; Showman et al. 2008). As shown in idealized dynamical models by Perez-Becker & Showman (2013), atmospheres with greater radiative time constants exhibit smaller day–night thermal contrasts.

Comparing the wide-band occultation depths measured here to the spectral atmospheric models of Fortney et al. (2008) and Burrows et al. (2008) shows that our measurements are better described by models that include an atmospheric inversion and a weak day–night energy circulation. As can be seen in Figure 11, the current atmospheric spectral models underestimate the occultation depth in the optical. Because the *Kepler* occultation depth measurement is of much higher precision than occultation depths measured here in other bands and than other occultations in the optical in other studies involving *Kepler* data (e.g., Désert et al. 2011a, 2011b; Fortney et al. 2011), this discrepancy could be attributed to the limits of the one-dimensional spectral models. If the *Kepler* band measurement uncertainty was similar to that in the other bands, then it would have been consistent with the models. Still, the fact that all models underestimate the *Kepler* occultation depth suggests a higher geometric albedo in the optical than the typical 0.050.10 predicted by the models. This supports the high geometric albedo of $A_g = 0.33^{+0.04}_{-0.06}$ derived in Section 3.1 for the equivalent blackbody object showing the same occultation depths. If indeed the Kepler-13Ab day-side atmosphere has a high A_g then this could be used as a clue to identify the material dominating the day-side reflectivity, along with the day-side temperature and the possible existence of atmospheric inversion.

Short-period planets are expected to reach full orbital circularization and spin-orbit synchronization due to tidal interaction with the host star, an interaction that grows stronger with decreasing period (e.g., Mazeh 2008). However, our measurement of the midoccultation time suggests a possible small but finite orbital eccentricity (see Section 2.4.1). If confirmed, it can lead to a nonsynchronized planetary rotation (e.g., Correia & Laskar 2011), meaning the day and night sides are not permanent, which could explain the small brightness temperature difference detected between them in the optical.

Our comparison between the atmospheres of Kepler-13Ab and WASP-33b shows that despite the similarity between the host stars and other similarities between the two star–planet systems, the planetary atmospheres seem to be different. If confirmed, it is yet another example of the diversity of exoplanets and exoplanet atmospheres, emphasizing the need to discover more exoplanets that allow the study of their atmosphere, in particular those orbiting early-type stars like the one investigated

here. Although spectra of such stars (currently) do not allow for high-precision RV measurements, preventing precise planet mass measurement (but see Galland et al. 2005; Lagrange et al. 2009), the planetary nature of massive close-in planets can be confirmed with high-quality space-based photometry of bright stars. This was done using *Kepler* data for Kepler-13Ab and can potentially be done in the future with data from the NASA K2 mission (Howell et al. 2014), the NASA transiting exoplanet survey satellite (TESS) mission,[30] and the European space agency (ESA) planetary transits and oscillations of stars (PLATO) mission (Rauer et al. 2013). In addition, detailed follow-up studies are also possible, like the measurement of stellar obliquity (Collier Cameron et al. 2010) and investigation of the planet atmosphere. The host star's increased mass, radius, temperature, and younger age, compared to Sun-like stars, will allow testing of planet formation and evolution theory.

A.S. thanks Ehud Nakar and Jason Eastman for enlightening discussions. This work was performed in part at the Jet Propulsion Laboratory, under contract with the California Institute of Technology (Caltech) funded by NASA through the Sagan Fellowship Program executed by the NASA Exoplanet Science Institute. J.G.O. receives support from the National Science Foundation's Graduate Research Fellowship Program. Gy.M.Sz. was supported by the Hungarian OTKA grants 104607 and 83790, the HUMAN MB08C 81013 grant of the MAG Zrt, and the János Bolyai Research Fellowship and a Lendület-2009 grant of the Hungarian Academy of Sciences. M.Z. is supported by the Center for Exoplanets and Habitable Worlds (CEHW) at the Pennsylvania State University. The Palomar/WIRC observation was in part supported by NASA through the American Astronomical Society's Small Research Grant program. This research has made use of NASA's Astrophysics Data System Service. This work is based on observations made by the *Spitzer Space Telescope*, which is operated by the Jet Propulsion Laboratory, California Institute of Technology, under a contract with NASA. The Palomar 200 inch (5 m) Hale Telescope (P200) is operated by Caltech, JPL, and Cornell University. Kepler was competitively selected as the tenth NASA Discovery mission. Funding for this mission is provided by the NASA Science Mission Directorate. Some of the data presented herein were obtained at the W. M. Keck Observatory, which is operated as a scientific partnership among the California Institute of Technology, the University of California, and the National Aeronautics and Space Administration. The Keck Observatory was made possible by the generous financial support of the W. M. Keck Foundation.

Facilities: Warm *Spitzer*, P200/WIRC, *Kepler*, Keck/HIRES, P200/PHARO

REFERENCES

Adams, E. R., Ciardi, D. R., Dupree, A. K., et al. 2012, AJ, 144, 42
Agol, E., Cowan, N. B., Knutson, H. A., et al. 2010, ApJ, 721, 1861
Barclay, T., Huber, D., Rowe, J. F., et al. 2012, ApJ, 761, 53
Barnes, J. W. 2009, ApJ, 705, 683
Barnes, J. W., Linscott, E., & Shporer, A. 2011, ApJS, 197, 10
Batalha, N. M., Rowe, J. F., Bryson, S. T., et al. 2013, ApJS, 204, 24
Bertelli, G., Girardi, L., Marigo, P., & Nasi, E. 2008, A&A, 484, 815
Bertelli, G., Nasi, E., Girardi, L., & Marigo, P. 2009, A&A, 508, 355
Bloemen, S., Marsh, T. R., Degroote, P., et al. 2012, MNRAS, 422, 2600
Borucki, W. J., Koch, D. G., Basri, G., et al. 2011, ApJ, 736, 19
Bouchy, F., Bonomo, A. S., Santerne, A., et al. 2011a, A&A, 533, A83
Bouchy, F., Deleuil, M., Guillot, T., et al. 2011b, A&A, 525, A68
Burrows, A. 2013, arXiv:1312.2009 (PNAS, accepted)
Burrows, A., Budaj, J., & Hubeny, I. 2008, ApJ, 678, 1436
Carter, J. A., Rappaport, S., & Fabrycky, D. 2011, ApJ, 728, 139
Carter, J. A., & Winn, J. N. 2009, ApJ, 704, 51
Claret, A., & Bloemen, S. 2011, A&A, 529, A75
Collier Cameron, A., Guenther, E., Smalley, B., et al. 2010, MNRAS, 407, 507
Correia, A. C. M., & Laskar, J. 2011, in Exoplanets, ed. S. Seager (Tucson, AZ: Univ. of Arizona Press), 239
Coughlin, J. L., & López-Morales, M. 2012, AJ, 143, 39
Cowan, N. B., & Agol, E. 2011, ApJ, 729, 54
Cowan, N. B., Fuentes, P. A., & Haggard, H. M. 2013, MNRAS, 434, 2465
Deming, D., Fraine, J. D., Sada, P. V., et al. 2012, ApJ, 754, 106
de Mooij, E. J. W., Brogi, M., de Kok, R. J., et al. 2013, A&A, 550, A54
Demory, B.-O., de Wit, J., Lewis, N., et al. 2013, ApJL, 776, L25
Demory, B.-O., Seager, S., Madhusudhan, N., et al. 2011, ApJL, 735, L12
Désert, J.-M., Charbonneau, D., Demory, B.-O., et al. 2011a, ApJS, 197, 14
Désert, J.-M., Charbonneau, D., Fortney, J. J., et al. 2011b, ApJS, 197, 11
de Wit, J., Gillon, M., Demory, B.-O., & Seager, S. 2012, A&A, 548, A128
Eastman, J., Siverd, R., & Gaudi, B. S. 2010, PASP, 122, 935
Ehrenreich, D., Lagrange, A.-M., Bouchy, F., et al. 2011, A&A, 525, A85
Esteves, L. J., De Mooij, E. J. W., & Jayawardhana, R. 2013, ApJ, 772, 51
Evans, T. M., Pont, F., Sing, D. K., et al. 2013, ApJL, 772, L16
Faigler, S., & Mazeh, T. 2011, MNRAS, 415, 3921
Faigler, S., Tal-Or, L., Mazeh, T., Latham, D. W., & Buchhave, L. A. 2013, ApJ, 771, 26
Fortney, J. J., Demory, B.-O., Désert, J.-M., et al. 2011, ApJS, 197, 9
Fortney, J. J., Lodders, K., Marley, M. S., & Freedman, R. S. 2008, ApJ, 678, 1419
Fulton, B. J., Shporer, A., Winn, J. N., et al. 2011, AJ, 142, 84
Galland, F., Lagrange, A.-M., Udry, S., et al. 2005, A&A, 443, 337
Gillon, M., Demory, B.-O., Barman, T., et al. 2007, A&A, 471, L51
Groot, P. J. 2012, ApJ, 745, 55
Hartman, J. D. 2010, ApJL, 717, L138
Hauschildt, P. H., Allard, F., & Baron, E. 1999, ApJ, 512, 377
Hayward, T. L., Brandl, B., Pirger, B., et al. 2001, PASP, 113, 105
Heng, K., & Demory, B.-O. 2013, ApJ, 777, 100
Herrero, E., Morales, J. C., Ribas, I., & Naves, R. 2011, A&A, 526, L10
Hoaglin, D. C., Mosteller, F., & Tukey, J. W. (ed.) 1983, Wiley Series in Probability and Mathematical Statistics (New York: Wiley)
Howell, S. B., Sobeck, C., Haas, M., et al. 2014, PASP, accepted (arXiv:1402.5163)
Husser, T.-O., Wende-von Berg, S., Dreizler, S., et al. 2013, A&A, 553, A6
Iro, N., Bézard, B., & Guillot, T. 2005, A&A, 436, 719
Jackson, B. K., Lewis, N. K., Barnes, J. W., et al. 2012, ApJ, 751, 112
Kaplan, D. L. 2010, ApJL, 717, L108
Kipping, D., & Bakos, G. 2011, ApJ, 730, 50
Knutson, H. A., Charbonneau, D., Allen, L. E., et al. 2007, Natur, 447, 183
Knutson, H. A., Howard, A. W., & Isaacson, H. 2010, ApJ, 720, 1569
Knutson, H. A., Lewis, N., Fortney, J. J., et al. 2012, ApJ, 754, 22
Kovács, G., Kovács, T., Hartman, J. D., et al. 2013, A&A, 553, A44
Lagrange, A.-M., Desort, M., Galland, F., Udry, S., & Mayor, M. 2009, A&A, 495, 335
Latham, D. W., Borucki, W. J., Koch, D. G., et al. 2010, ApJL, 713, L140
Law, N. M., Morton, T., Baranec, C., et al. 2013, arXiv:1312.4958
Lewis, N. K., Knutson, H. A., Showman, A. P., et al. 2013, ApJ, 766, 95
Loeb, A. 2005, ApJL, 623, L45
Loeb, A., & Gaudi, B. S. 2003, ApJL, 588, L117
Madhusudhan, N. 2012, ApJ, 758, 36
Madhusudhan, N., Mousis, O., Johnson, T. V., & Lunine, J. I. 2011, ApJ, 743, 191
Madhusudhan, N., & Seager, S. 2009, ApJ, 707, 24
Madhusudhan, N., & Seager, S. 2010, ApJ, 725, 261
Mandel, K., & Agol, E. 2002, ApJL, 580, L171
Mazeh, T. 2008, in Observational Evidence for Tidal Interaction in Close Binary Systems, ed. M. J. Goupil & J. P. Zahn, EAS Publ. Ser., 29, 1
Mazeh, T., Nachmani, G., Sokol, G., Faigler, S., & Zucker, S. 2012, A&A, 541, A56
Mighell, K. J. 2005, MNRAS, 361, 861
Mislis, D., & Hodgkin, S. 2012, MNRAS, 422, 1512
Monnier, J. D., Zhao, M., Pedretti, E., et al. 2007, Sci, 317, 342
Morris, S. L. 1985, ApJ, 295, 143
Morris, S. L., & Naftilan, S. A. 1993, ApJ, 419, 344
Moya, A., Bouy, H., Marchis, F., Vicente, B., & Barrado, D. 2011, A&A, 535, A110
O'Rourke, J. G., Knutson, H. A., Zhao, M., et al. 2014, ApJ, 781, 109

[30] Scheduled for launch in 2017, see http://tess.gsfc.nasa.gov.

Perez-Becker, D., & Showman, A. P. 2013, ApJ, 776, 134
Perna, R., Heng, K., & Pont, F. 2012, ApJ, 751, 59
Pfahl, E., Arras, P., & Paxton, B. 2008, ApJ, 679, 783
Pickles, A., & Depagne, É. 2010, PASP, 122, 1437
Placek, B., Knuth, K. H., & Angerhausen, D. 2013, arXiv:1310.6764
Rauer, H., Catala, C., Aerts, C., et al. 2013, arXiv:1310.0696
Rowe, J. F., Matthews, J. M., Seager, S., et al. 2008, ApJ, 689, 1345
Santerne, A., Moutou, C., Barros, S. C. C., et al. 2012, A&A, 544, L12
Sharp, C. M., & Burrows, A. 2007, ApJS, 168, 140
Showman, A. P., Cooper, C. S., Fortney, J. J., & Marley, M. S. 2008, ApJ, 682, 559
Showman, A. P., Fortney, J. J., Lian, Y., et al. 2009, ApJ, 699, 564
Showman, A. P., & Guillot, T. 2002, A&A, 385, 166
Shporer, A., Brown, T., Mazeh, T., & Zucker, S. 2012, NewA, 17, 309
Shporer, A., Jenkins, J. M., Rowe, J. F., et al. 2011, AJ, 142, 195
Shporer, A., Kaplan, D. L., Steinfadt, J. D. R., et al. 2010, ApJL, 725, L200
Shporer, A., Mazeh, T., Pont, F., et al. 2009, ApJ, 694, 1559
Smith, A. M. S., Anderson, D. R., Skillen, I., Collier Cameron, A., & Smalley, B. 2011, MNRAS, 416, 2096
Still, M., & Barclay, T. 2012, Astrophysics Source Code Library, 8004
Szabó, G. M., Pál, A., Derekas, A., et al. 2012, MNRAS, 421, L122
Szabó, G. M., Simon, A., & Kiss, L. L. 2014, MNRAS, 437, 1045
Szabó, G. M., Szabó, R., Benkő, J. M., et al. 2011, ApJL, 736, L4
Todorov, K. O., Deming, D., Knutson, H. A., et al. 2012, ApJ, 746, 111
van Kerkwijk, M. H., Rappaport, S. A., Breton, R. P., et al. 2010, ApJ, 715, 51
Vogt, S. S., Allen, S. L., Bigelow, B. C., et al. 1994, Proc. SPIE, 2198, 362
von Essen, C., Czesla, S., Wolter, U., et al. 2014, A&A, 561, A48
Williams, P. K. G., Charbonneau, D., Cooper, C. S., Showman, A. P., & Fortney, J. J. 2006, ApJ, 649, 1020
Wilson, J. C., Eikenberry, S. S., Henderson, C. P., et al. 2003, Proc. SPIE, 4841, 451
Winn, J. N. 2011, in Exoplanets, ed. S. Seager (Tucson, AZ: Univ. of Arizona Press), 55
Zhao, M., Milburn, J., Barman, T., et al. 2012a, ApJL, 748, L8
Zhao, M., Monnier, J. D., Swain, M. R., Barman, T., & Hinkley, S. 2012b, ApJ, 744, 122
Zucker, S., Mazeh, T., & Alexander, T. 2007, ApJ, 670, 1326